

# Understanding the computation of time using neural network models

Zedong Bi<sup>a,b</sup> and Changsong Zhou<sup>b,c,d,e,1</sup>

<sup>a</sup>Institute for Future, Qingdao University, Shandong 266071, China

<sup>b</sup>Department of Physics, Centre for Nonlinear Studies and Institute of Computational and Theoretical Studies, Hong Kong Baptist University, Kowloon Tong, Hong Kong, China

<sup>c</sup>Research Centre, HKBU Institute of Research and Continuing Education, Shenzhen, China

<sup>d</sup>Beijing Computational Science Research Center, Beijing, China

<sup>e</sup>Department of Physics, Zhejiang University, 38 Zheda Road, Hangzhou, China

<sup>1</sup>E-mail: cszhou@hkbu.edu.hk

November 20, 2021

## Abstract

To maximize future rewards in this ever-changing world, animals must be able to discover the temporal structure of stimuli and then anticipate or act correctly at the right time. How the animals perceive, maintain, and use time intervals ranging from hundreds of milliseconds to multi-seconds in working memory? How temporal information is processed concurrently with spatial information and decision making? Why there are strong neuronal temporal signals in tasks in which temporal information is not required? A systematic understanding of the underlying neural mechanisms is still lacking. Here, we addressed these problems using supervised training of recurrent neural network models. We revealed that neural networks perceive elapsed time through state evolution along stereotypical trajectory, maintain time intervals in working memory in the monotonic increase or decrease of the firing rates of interval-tuned neurons, and compare or produce time intervals by scaling state evolution speed. Temporal and non-temporal information are coded in subspaces orthogonal with each other, and the state trajectories with time at different non-temporal information are quasi-parallel and isomorphic. Such coding geometry facilitates the decoding generalizability of temporal and non-temporal information across each other. The network structure exhibits multiple feedforward sequences that mutually excite or inhibit depending on whether their preferences of non-temporal information are similar or not. We identified four factors that facilitate strong temporal signals in non-timing tasks, including the anticipation of coming events. Our work discloses fundamental computational principles of temporal processing, and is supported by and gives predictions to a number of experimental phenomena.

**Keywords**— interval timing | population coding | neural network model

## Significance

Perceiving, maintaining, and using time intervals in working memory are crucial for animals to anticipate or act correctly at the right time in the ever-changing world. Here we systematically study the underlying neural mechanisms by training recurrent neural networks to perform temporal tasks or complex tasks in combination with spatial information processing and decision making. We found that neural networks perceive time through state evolution along stereotypical trajectories, and produce time intervals by scaling evolution speed. Temporal and non-temporal information are jointly coded in a way that facilitates decoding generalizability. We also provided potential sources for the temporal signals observed in non-timing tasks. Our study revealed the computational principles of a number of experimental phenomena and provided several novel predictions.

## Introduction

Much information that the brain processes and stores is temporal in nature. Therefore, to understand the processing of time in the brain is of fundamental importance in neuroscience [1, 2, 3, 4]. To predict and maximize future rewards in this ever-changing world, animals must be able to discover the temporal structure of stimuli and then flexibly anticipate or act correctly at the right time. To this end, animals must be able to perceive, maintain, and then use time intervals in working memory, appropriately combining the processing of time with spatial information and decision making. Based on behavioral data and the diversity of neuronal response profiles, it has been proposed [5, 6] that time intervals in the range of hundreds of milliseconds to multi-seconds can be decoded through neuronal population states evolving along transient trajectories. The neural mechanisms may be accumulating firing [7, 8], synfire chains [9, 10], the beating of a range of oscillation frequencies [11], etc. However, these mechanisms are challenged by recent finding that animals can flexibly adjust the evolution speed of population activity along an invariant trajectory to produce different intervals [12]. Through behavioral experiments, it was found that humans can store time intervals as distinct items in working memory in a resource allocation strategy [13], but an electrophysiological

arXiv:1910.05546v4 [q-bio.NC] 7 Jul 2020

study on the neuronal coding of time intervals maintained in working memory is still lacking. Moreover, increasing evidence indicates that timing does not rely on dedicated circuits in the brain, but instead is an intrinsic computation that emerges from the inherent dynamics of neural circuits [14, 3]. Spatial working memory and decision making are believed to rely mostly on a prefronto-parietal circuit [15, 16]. The dynamics and the network structure that enable this circuit to combine spatial working memory and decision making with flexible timing remains unclear. Overall, our understanding of the processing of time intervals in the brain is fragmentary and incomplete. It is therefore essential to develop a systematic understanding of the fundamental principle of temporal processing and its combination with spatial information processing and decision making.

The formation of temporal signals in the brain is another unexplored question. Strong temporal signals were found in the brain even when monkeys performed working memory tasks where temporal information was not needed [17, 18, 19, 20, 21]. In a vibrotactile working memory task [17], monkeys were trained to report which of the two vibrotactile stimuli separated by a fixed-delay period had higher frequency (**Fig. 1d**). Surprisingly, although the duration of the delay period was not needed to perform this task, temporal information was still coded in the neuronal population state during the delay period, with the time-dependent variance explaining more than 75% of the total variance [18, 19]. Similar scenario was also found in other non-timing working memory tasks [19, 20, 21]. It is unclear why so strong temporal signals arised in non-timing tasks.

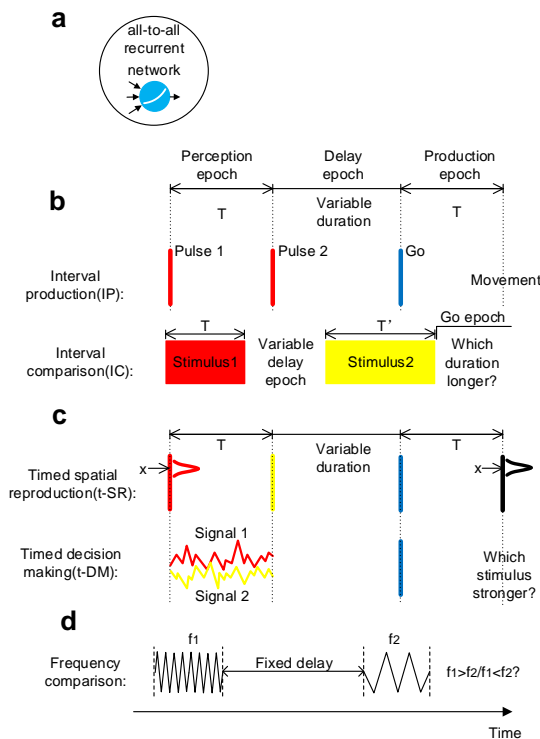


Figure 1: **Model setup.** (a) All-to-all connected recurrent networks with softplus units are trained. (b) Basic timing tasks. IP: The duration  $T$  of the perception epoch determines the movement time after the Go cue. IC: The duration  $T$  of the stimulus1 epoch is compared with the duration  $T'$  of the stimulus2 epoch. Stimuli with different colors (red, yellow, or blue) indicate that they are input to the network through different synaptic weights. (c) Combined timing tasks.  $T$  determines the movement time after the Go cue. Spatial location (t-SR) or decision choice (t-DM) determines the movement behavior. (d) A non-timing task in the experimental study [18]. Although the duration of the delay period is not needed to perform the task, there exists strong temporal signals in the delay period.

Previous works showed that after being trained to perform tasks such as categorization, working memory, decision making, and motion generation, artificial neural networks (ANN) exhibited coding or dynamic properties surprisingly similar to experimental observations [22, 23, 24, 25]. Compared with animal experiments, ANN can cheaply and easily implement a series of tasks, greatly facilitating the test of various hypotheses and the capture of common underlying computational principles [26, 27]. In this paper, we trained recurrent neural networks (**Fig. 1a**) to study the processing of temporal information. Firstly, by training networks on basic timing tasks which require only temporal information to perform (**Fig. 1b**), we studied how time intervals are perceived, maintained, and used in working memory. Secondly, by training networks on combined timing tasks which require both temporal and non-temporal information to perform (**Fig. 1c**), we studied how the processing of time is combined with spatial information processing and decision making, the influence of this combination to decoding generalizability, and the network structure that this combination is based on. Thirdly, by training networks on non-timing tasks (**Fig. 1d**), we studied why so large time-dependent variance arises in non-timing tasks, thereby understanding the factors that facilitate the formation of temporal signals in the brain. Our work presents a thorough understanding of the neural computation of time.

# Results

We trained a recurrent neural network (RNN) of 256 softplus units supervisedly using back-propagation through time. Self-connections of the RNN were initialized to 1, and off-diagonal connections were initialized as independent Gaussian variables with mean 0 [27], with different training configurations initialized using different random seeds. The strong self-connections supported self-sustained activity after training (**Fig. S1b**), and the non-zero initialization of the off-diagonal connections induced sequential activity comparable to experimental observations [27]. We stopped training as soon as the performance of the network reached criterion [23, 25] (see performance examples in **Fig. S1**).

## Basic timing tasks: interval production and interval comparison tasks

### Interval production task

In the interval production (IP) task (the first task of **Fig. 1b**), the network was to perceive the interval  $T$  between the first two pulses, maintain the interval during the delay epoch with variable duration, and then produce an action at time  $T$  after the Go cue. Neuronal activities after training exhibited strong fluctuations (**Fig. 2a**). In the following, we report on the dynamics of the network in the perception, delay and production epochs of IP (see **Fig. 1** for illustration of these epochs).

The first epoch is the perception epoch. In response to the first stimulus pulse, the network started to evolve from almost the same state along an almost identical trajectory in different simulation trials with different  $T$  values until another pulse came (**Fig. 2b**); the activities of individual neurons before the second pulse in different trials highly overlapped (**Fig. 2c, d**). Therefore, the network state evolved along a stereotypical trajectory starting from the first pulse, and the time interval  $T$  between the first two pulses can be read out using the position in this trajectory when the second pulse came. Behaviorally, a human’s perception of the time interval between two acoustic pulses is impaired if a distractor pulse appears shortly before the first pulse [28]. A modeling work [28] explained that this is because successful perception requires the network state to start to evolve from near a state  $\mathbf{s}_0$  in response to the first pulse, whereas the distractor pulse kicks the network state far away from  $\mathbf{s}_0$ . This explanation is consistent with our results that interval perception requires a stereotypical trajectory.

We then studied how the information of timing interval  $T$  between the first two pulses was maintained during the delay epoch. We have the following findings. (1) The speeds of the trajectories decreased with time in the delay epoch (**Fig. 2e, f**). (2) The states  $\mathbf{s}_{\text{EndDelay}}$  at the end of the delay epoch at different  $T$ s were aligned in a manifold  $\mathcal{M}$  whose first PC explained 90% of its variance (**Fig. 2g**). (3) For a specific simulation trial, the position of  $\mathbf{s}_{\text{EndDelay}}$  in manifold  $\mathcal{M}$  linearly encoded the  $T$  value of the trial (**Fig. 2h**). (4) The distance between two adjacent trajectories kept almost unchanged with time during the delay, neither decayed to zero, nor exploded (**Fig. 2i**): this stable dynamics supported the information of  $T$  encoded by the position in the stereotypical trajectory at the end of the perception epoch in being maintained during the delay. Collectively,  $\mathcal{M}$  approximated a line attractor [29, 24] with slow dynamics, and  $T$  was encoded as the position in  $\mathcal{M}$ . To better understand the scheme of coding  $T$  in  $\mathcal{M}$ , we classified neuronal activity  $f(T)$  in manifold  $\mathcal{M}$  as a function of  $T$  into three types (**Fig. 2j, k**): monotonically decreasing (MoD), monotonically increasing (MoI), and non-monotonic (non-M) (see Methods). We found that most neurons were MoD or MoI, whereas only a small portion were non-M neurons (**Fig. 2k**). This implies that the network mainly used a complementary (i.e., concurrently increasing and decreasing) monotonic scheme to code time intervals in the delay epoch, similar to the scheme revealed in Ref. [30, 17]. This dominance of monotonic neurons may be the reason why the first PC of  $\mathcal{M}$  explained so much variance (**Fig. 2g**), see Section S2 and **Figs. S2g, h** for a simple explanation.

In the production epoch, the trajectories of the different  $T$  values tended to be isomorphic (**Fig. 2l**). The neuronal activity profiles were self-similar when stretched or compressed in accordance with the produced interval (**Fig. 2m**), suggesting temporal scaling with  $T$  [12]. To quantify this temporal scaling, we defined the scaling index (SI) of a subspace  $\mathcal{S}$  as the portion of variance of the projections of trajectories into  $\mathcal{S}$  that can be explained by temporal scaling [12]. We found that the distribution of SI of individual neurons aggregated toward 1 (**Fig. S2b**), and the first two PCs that explained most variance have the highest SI (**Fig. S2c**). We then used a dimensionality reduction technique that furnished a set of orthogonal directions (called scaling components, or SCs) in the network state space that were ordered according to their SI (see Methods). We found that a subspace (spanned by the first three SCs) that had high SI (=0.98) occupied about 40% of the total variance of trajectories (**Fig. 2n**), in contrast with the low SI of the perception epoch (**Fig. S2f**). The average speed of the trajectory in the subspace of the first three SCs was inversely proportional to  $T$  (**Fig. 2o**). Collectively, the network adjusted its dynamic speed to produce different time intervals in the production epoch, similar to observations of the medial frontal cortex of monkeys [31, 12]. Additionally, we found a non-scaling subspace whose mean activity during the production epoch changed linearly with  $T$  (**Fig. S2d, e**), also similar to the experimental observations in Ref. [31, 12].

### Interval comparison task

In the interval comparison (IC) task (the second task of **Fig. 1b**), the network was successively presented two intervals; it was then required to judge which interval was longer. IC required the network to perceive the time interval  $T$  of the stimulus1 epoch, to maintain the interval in the delay epoch, and to use it in the stimulus2 epoch whose duration is  $T'$ . Similar to IP, the network perceived time interval with a stereotypical trajectory in the stimulus1 epoch (**Fig. S3a-c**) and maintained time interval using attractor dynamics with a complementary monotonic coding scheme in the delay epoch (**Fig. S3d-h**). The trajectory in the stimulus2 epoch had a critical point  $\mathbf{s}_{\text{crit}}$  at time  $T$  after the start of stimulus 2. The network was to give different comparison outputs at the Go epoch depending on whether or not the trajectory had passed  $\mathbf{s}_{\text{crit}}$  at the end of stimulus 2. To make a correct comparison choice, only the period from the start of stimulus 2 to  $\mathbf{s}_{\text{crit}}$  (or to the end of stimulus 2 if  $T > T'$ ) need to be timed: as long as the trajectory had passed  $\mathbf{s}_{\text{crit}}$ , the network could readily make the decision that  $T < T'$ , with no more timing required. After training, we studied the trajectories from the start of stimulus 2 to  $\mathbf{s}_{\text{crit}}$  in the cases that  $T < T'$ , and found temporal scaling (**Fig. S3j-n**) similar to the production epoch of IP, consistently with animal experiments [32, 33]. These similarities between IP and IC on how to perceive, maintain and use time intervals imply universal computational schemes for neural networks to process temporal information.

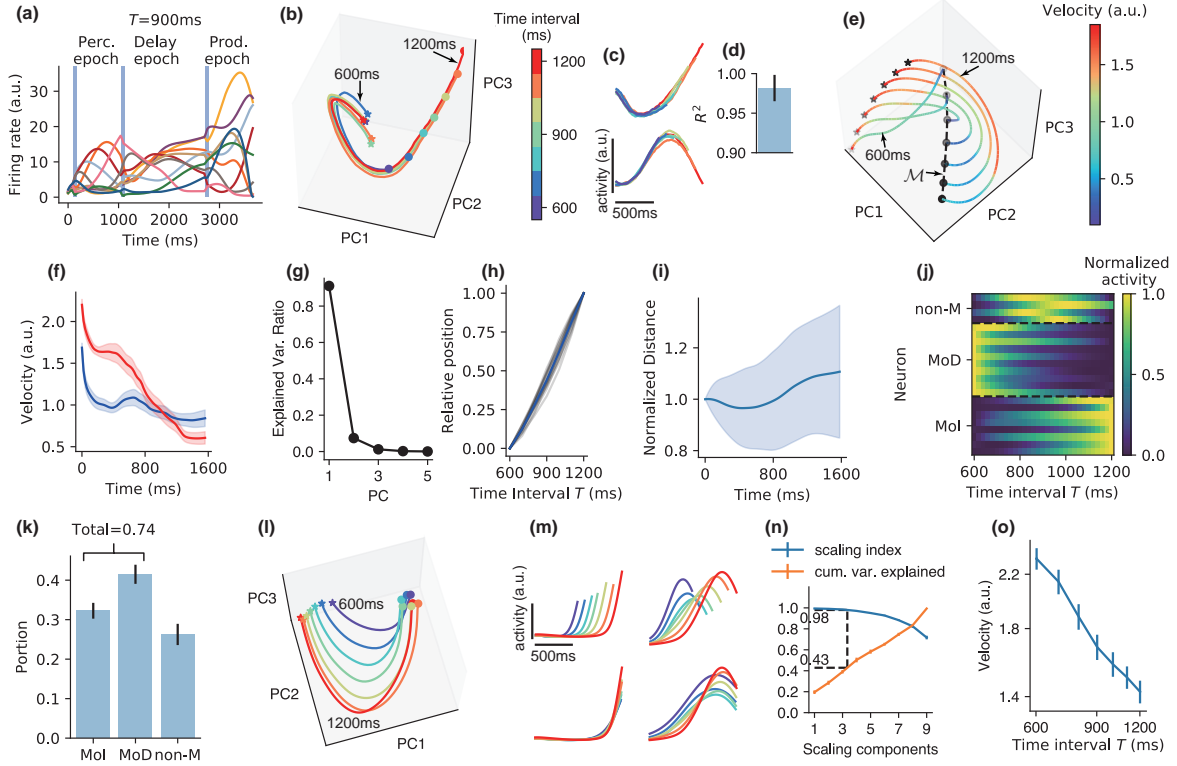


**Figure 2: Interval production task.** (a) The activities of example neurons (indicated by lines of different colors) when the time interval  $T$  between the first two pulses is 900 ms. Vertical blue shadings indicate the pulses input to the network. (b) Population activity in the perception epoch in the subspace of the first three PCs. Colors indicate the time interval  $T$ . Stars and circles respectively indicate the starting and ending points of the perception epoch. The trajectories for  $T = 600$  ms and 1200 ms are labeled. (c) Firing profiles of two example neurons in the perception epoch. Line colors have the same meaning as in panel b. (d) Coefficient of determination ( $R^2$ ) of how much the neuronal firing profile with the largest  $T$  can explain the variance of the firing profiles with smaller  $T$  in the perception epoch. Error bar indicates s.d. over different neurons and  $T$  values. (e) Population activity in the subspace of the first three PCs in the delay epoch. Colors indicate trajectory speed. The increasing blackness of stars and circles indicates trajectories with  $T = 600$  ms, 700 ms, ..., 1200 ms. The dashed curve connecting the end points of the delay epoch marks manifold  $\mathcal{M}$ . (f) Trajectory speed as a function of time in the delay epoch when  $T = 600$  ms (blue) and 1200 ms (red). Shaded belts indicate s.e.m. (standard error of mean) over training configurations. (g) Ratio of explained variance of the first five PCs of manifold  $\mathcal{M}$ . Error bars that indicate s.e.m. are smaller than plot markers. (h) The position of the state at the end of the delay epoch projected in the first PC of manifold  $\mathcal{M}$  as a function of  $T$ . The position when  $T = 600$  ms (or 1200 ms) is normalized to be 0 (or 1). Gray curves: 16 training configurations. Blue curve: mean value. (i) The distance between two adjacent curves in the delay epoch as a function of time, with the distance at the beginning of the delay epoch normalized to be 1. Shaded belts indicate standard deviation. (j) Firing rates of example neurons of monotonically decreasing (MoD), monotonically increasing (MoI), and non-monotonic (non-M) types as functions of  $T$  in manifold  $\mathcal{M}$ . (k) The portions of the three types of neurons. (l) Population activity in the production epoch in the subspace of the first three PCs. Colors indicate the time intervals to be produced, as shown in the color bar of panel b. Stars and circles respectively indicate the starting and ending points of the production epoch. (m) Upper: firing profiles of two example neurons in the production epoch. Lower: firing profiles of the two neurons after temporally scaled according to produced intervals. (n) A point at horizontal coordinate  $x$  means the scaling index (blue) or ratio of explained variance (orange) of the subspace spanned by the first  $x$  scaling components (SCs). Dashed lines indicate that a subspace with scaling index 0.98 explains, on average, 43% of the total variance. (o) Trajectory speed in the subspace of the first three SCs as the function of the time interval to be produced. In panels k, n, o, error bars indicate s.e.m. over training configurations. During training, we added recurrent and input noises (see Methods). Here and in the following, when analyzing the network properties after training, we turned off noises by default. We kept noises for the perception epoch in panels b, c, d. Without noise, the trajectories in the perception epoch would fully overlap under different  $T$ s.

The average speed of the trajectory after  $s_{crit}$  increased with  $T$  (**Fig. S3o**), whereas the speed before  $s_{crit}$  decreased with  $T$ : this implies that the dynamics after  $s_{crit}$  was indeed different from that before.

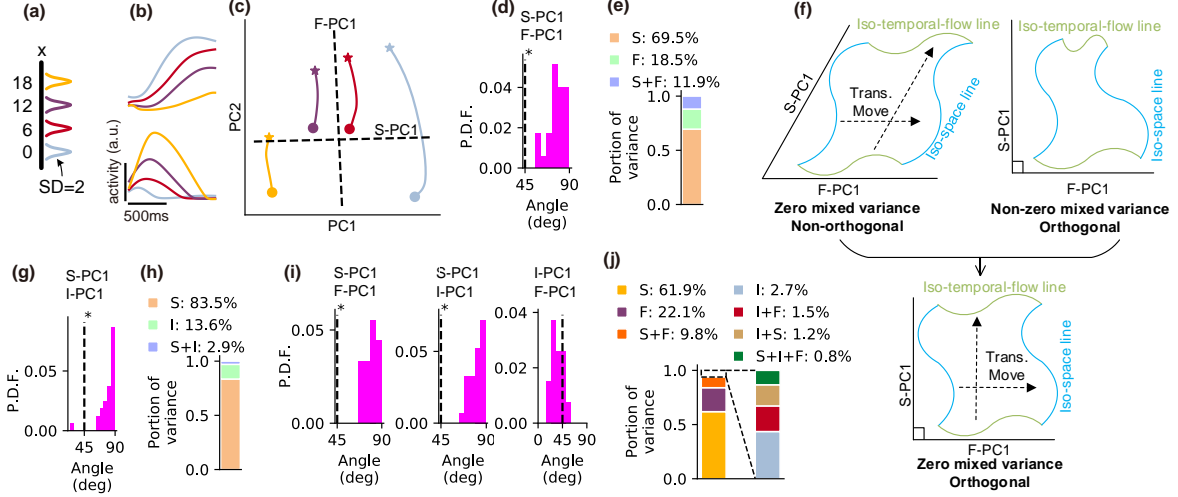


Figure 3: **Timed spatial reproduction task.** (a) Color scheme that represents the spatial location of the first pulse, used in panels b, c. Location is represented by Gaussian bump with standard deviation 2. (b) Firing profiles of four example neurons in the perception epoch. (c) Trajectory of the perception epoch in the subspace of the first two PCs. Stars indicate the points after 400 ms of transient period from the beginning of the perception epoch, and circles indicate the ending points of the perception epoch. Dashed lines represent the projections of F-PC1 and S-PC1 in this subspace. (d) Probability distribution function (p.d.f.) of the angle between F-PC1 and S-PC1 in the perception epoch over 32 training configurations. Asterisk indicates significant ( $p < 0.05$ ) larger than  $45^\circ$  (t test). (e) Portion of variance explained by spatial information (S), temporal flow (F) and their mixture (S+F) in the perception epoch, averaging over 32 training configurations. (f) Schematic for the meanings of angle and mixed variance. Zero mixed variance implies that different iso-space (blue) or iso-temporal-flow (green) lines are related by translational movement, forming parallelogram-like grids (upper left), together with orthogonality (upper right) implies rectangle-like grids (lower). (g) The distribution of the angle between I-PC1 and S-PC1 in manifold  $\mathcal{M}$  (**Fig.2e**) at the end of the delay epoch. (h) The portion of variance explained by spatial information (S), time interval (I) and their mixture (S+I) in manifold  $\mathcal{M}$  at the end of the delay epoch. (i) The distributions of the angles between F-PC1, I-PC1 and S-PC1 in the production epoch. (j) The portion of variance explained by spatial information (S), temporal flow (F), time interval (I) and their mixtures in the production epoch. In **a-e**,  $T = 1200$  ms for the perception epoch; in **g-j**,  $T = 600$  ms, 700 ms, ..., 1200 ms for the delay and production epochs.

## Combined timing tasks: timed spatial reproduction and timed decision making tasks

It is a ubiquitous phenomenon that neural networks encode more than one quantities simultaneously [34, 35, 36]. In this subsection, we will discuss how neural networks encode temporal and spatial information (or decision choice) simultaneously, which enables the brain to take the right action at the right time.

### Timed spatial reproduction task

In the timed spatial reproduction (t-SR) task (the first task in **Fig. 1c**), the network was to not only take action at the desired time but also act at the spatial location indicated by the first pulse. Similar to IP and IC, the network used stereotypical trajectories, attractors and speed scaling to perceive, maintain and produce time intervals (**Fig. S4**). In the following, we will focus on the coding combination of temporal and spatial information.

In the perception epoch, under the two cases when the first pulse were at two locations  $x$  and  $y$  separately, the activities  $r_{i,perc}(t, x)$  and  $r_{i,perc}(t, y)$  of the  $i$ th neuron exhibited similar profiles with time  $t$  (**Fig. 3b**), especially when  $x$  and  $y$  had close values. In our simulation, the location of the first pulse was represented by a Gaussian bump with standard deviation 2, which is much smaller than the smallest spatial distance 6 between two different colors in **Fig. 3a, b**; thus, the similarity of the temporal profiles in **Fig. 3b** should not result from the overlap of the sensory inputs from the first pulse but rather emerge during training.

To quantitatively investigated the coding combination of temporal and spatial information, we studied the first temporal-flow PC (F-PC1) of the neuronal population, namely the first PC of  $\{\langle r_{i,perc}(t, x) \rangle_x\}_i$ , and the first spatial PC (S-PC1), namely the first PC of  $\{\langle r_{i,perc}(t, x) \rangle_t\}_i$ , with  $\langle \cdot \rangle_a$  indicating averaging over parameter  $a$ . By *temporal flow*, we mean the time elapsed from the beginning of a specific epoch. We found that the angle between F-PC1 and S-PC1 distributed around  $90^\circ$ , significantly larger than  $45^\circ$  (**Fig. 3d**). This indicates that temporal flow and spatial information was coded in almost orthogonal subspaces (**Fig. 3c**). We then studied the mixed variance [19]. Specifically, the variance explained by temporal (or spatial) information is  $v_t = \text{Var}_{i,t}(\langle r_{i,perc}(t, x) \rangle_x)$  (or  $v_x = \text{Var}_{i,x}(\langle r_{i,perc}(t, x) \rangle_t)$ ), and the mixed variance is  $v_{t+x} = v_{tot} - v_t - v_x$ , where  $v_{tot} = \text{Var}_{i,t,x}(r_{i,perc}(t, x))$  is the total variance. We found that the mixed variance took a small portion of the total

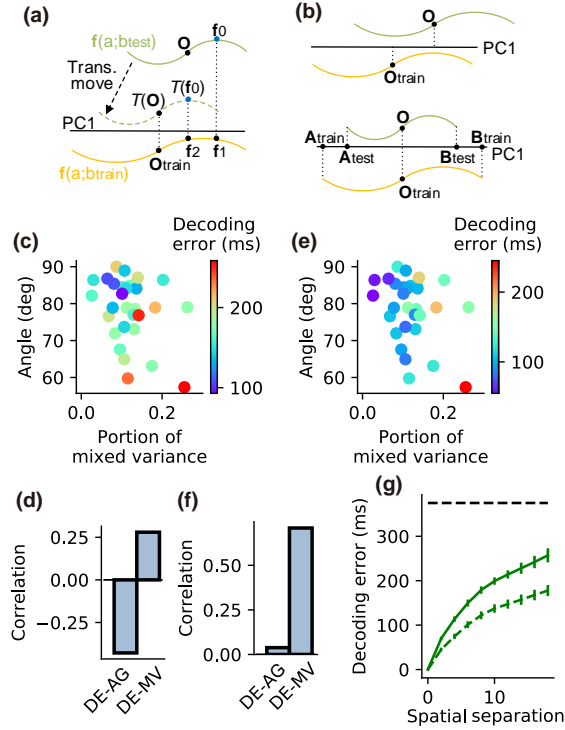


Figure 4: **Decoding generalizability.** (a) Schematic that explains Decoder 1 and Decoder 2. The decoders read the value of  $a$  through state  $f_0$  in iso- $b$  line  $f(a; b_{test})$  (green) after being trained by another iso- $b$  line  $f(a; b_{train})$  (orange). Decoder 1 reads  $a$  to be the same as that of  $f_1$ , because  $f_0$  and  $f_1$  project to the same point on PC1 (black horizontal line) of  $f(a; b_{train})$ . Decoder 2 first translationally moves  $f(a; b_{test})$  so that its mass center  $\mathcal{T}(O)$  after translational movement  $\mathcal{T}$  projects to the same point as the mass center  $O_{train}$  of  $f(a; b_{train})$  on PC1, and then reads  $a$  according to  $\mathcal{T}(f_0)$ , which is the  $a$  value of  $f_2$ . (b) Two error sources of Decoder 1. Upper: the mass centers  $O$  and  $O_{train}$  do not project to the same point on PC1. Lower: the projections of  $f(a; b_{train})$  and  $f(a; b_{test})$  on PC1 (lines  $A_{train}B_{train}$  and  $A_{test}B_{test}$ ) do not have the same length. (c) The error of Decoder 1 (indicated by dot color) to read temporal flow across different spatial locations as a function of the angle and mixed variance between the temporal-flow and spatial subspaces, in the production epoch of t-SR task. (d) Correlation between decoding error (DE) and angle (AG), and between DE and mixed variance (MV). (e,f) The same as c and d, except for Decoder 2. (g) Decoding error as a function of  $|x_{train} - x_{test}|$ , after Decoder 1 (solid line) or Decoder 2 (dashed line) is trained to read the temporal flow using the iso-space line at spatial location  $x_{train}$ , and then tested at spatial location  $x_{test}$ . Horizontal dashed line indicates chance level, supposing the decoder works by random guess. Error bars represent mean  $\pm$  s.e.m. across simulation trials. Panels c-f analyze the data averaging over  $|x_{train} - x_{test}|$  in individual training configurations.  $T = 1200$  ms. See decoding generalizability in other epochs of t-SR task and t-DM task in **Figs. S7, S8**.

variance, smaller than the variance of either temporal or spatial information (**Fig. 3e**). To understand the implication of this result, we noted that a sufficient condition for  $v_{t+x} = 0$  is that different iso-space (or iso-temporal-flow) lines are related with each other through translational movement (**Fig. 3f, upper left**), where an iso-space (or iso-temporal-flow) line is a manifold in the state space with different temporal flow (or space) values but a fixed space (or temporal flow) value; the opposite extreme case  $v_{t+x} = v_{tot}$  implies that different iso-space (or iso-temporal-flow) lines are strongly intertwined, see SI Text Section S3 for details. Together, orthogonality and small mixed variance suggest that iso-space and iso-time lines interweave into rectangle-like grids (**Fig. 3f, lower**), see **Fig. S6** for illustrations of the simulation results.

In the delay epoch, the population states were attracted toward a manifold  $\mathcal{M}$  of slow dynamics at the end of the delay epoch (**Fig. 2e-i** and **Fig. S4b-d**), maintaining both the duration  $T$  of the perception epoch and the spatial information  $x$ . We studied the coding combination of  $T$  and  $x$  in  $\mathcal{M}$  in a similar way to above. We found that the first time-interval PC (I-PC1), namely the first PC to code  $T$ , was largely orthogonal with the first spatial PC (S-PC1) (**Fig. 3g**), and the mixed variance between  $T$  and  $x$  was small (**Fig. 3h**).

In the production epoch, the network needed to maintain three information: temporal flow  $t$ , time interval  $T$ , and spatial location  $x$ . We studied the angle between the first PCs of any two of them (i.e., F-PC1, I-PC1 and S-PC1). We found that S-PC1 was orthogonal with F-PC1 and I-PC1, but F-PC1 and I-PC1 was not orthogonal (**Fig. 3i**). For any two parameters, their mixed variance was smaller than the variance of their own (**Fig. 3j**), see Methods for details.

Collectively, in all the three epochs, the coding subspaces of temporal and spatial information were largely orthogonal with small mixed variance, suggesting rectangle-like grids of iso-space and iso-time lines, see **Fig. S6** for illustrations.

## Timed decision making task

In the timed decision making (t-DM) task (the second task in **Fig. 1c**), the network was to make a decision choice at the desired time to indicate which of the two presented stimuli was stronger. Similar to IP, IC and t-SR, the network used stereotypical trajectories, attractors and speed scaling to separately perceive, maintain and produce time intervals (**Fig. S5a-m**). In all the three epochs of t-DM, the first PC to code decision choice (D-PC1) was orthogonal with F-PC1 or I-PC1, and the mixed variance between any two parameters were small (**Fig. S5n-s**); but F-PC1 and I-PC1 in the production epoch was not orthogonal (**Fig. S5r**). These results are all similar to those of t-SR task.

## Decoding generalizability

We then studied how the above geometry of coding space influences decoding generalizability: suppose the population state space is parameterized by  $a$  and  $b$ , we want to know the error of decoding  $a$  from a state  $\mathbf{f}_0$  in an iso- $b$  line  $\mathbf{f}(a; b_{test})$  after training the decoder using another iso- $b$  line  $\mathbf{f}(a; b_{train})$  (**Fig. 4a**). We considered two types of nearest-centroid decoders [20]: Decoder 1 projects both  $\mathbf{f}_0$  and  $\mathbf{f}(a; b_{train})$  into the first PC of  $\mathbf{f}(a; b_{train})$ , and reads the value of  $a$  to be the value that minimized the distance between  $\mathcal{P}_{dec}[\mathbf{f}(a; b_{train})]$  and  $\mathcal{P}_{dec}[\mathbf{f}_0]$ , where  $\mathcal{P}_{dec}[\cdot]$  indicates the projection operation; Decoder 2 first translationally moves the whole iso- $b$  line  $\mathbf{f}(a; b_{test})$  so that the mass center of  $\mathcal{P}_{dec}[\mathcal{T}[\mathbf{f}(a; b_{test})]]$  coincides with that of  $\mathcal{P}_{dec}[\mathbf{f}(a; b_{train})]$ , where  $\mathcal{T}$  indicates the translation operation, and then reads  $a$  according to  $\mathcal{P}_{dec}[\mathcal{T}[\mathbf{f}_0]]$  (**Fig. 4a**). Apparently, zero error of Decoder 1 requires  $\mathcal{P}_{dec}[\mathbf{f}(a; b_{test})]$  and  $\mathcal{P}_{dec}[\mathbf{f}(a; b_{train})]$  to perfectly overlap. If the grids woven by iso- $a$  and iso- $b$  lines are tilted (**Fig. 3f, upper left**) or non-parallelogram-like (**Fig. 3f, upper right**), which can be respectively quantified by the orthogonality or mixed variance ratio introduced in the above section, the projections  $\mathcal{P}_{dec}[\mathbf{f}(a; b_{test})]$  and  $\mathcal{P}_{dec}[\mathbf{f}(a; b_{train})]$  may have non-overlapping mass centers (**Fig. 4b, upper**) or different lengths (**Fig. 4b, lower**), causing decoding error. Decoder 2 translationally moves the mass center of  $\mathcal{P}_{dec}[\mathbf{f}(a; b_{test})]$  to the position of that of  $\mathcal{P}_{dec}[\mathbf{f}(a; b_{train})]$ , so its decoding error only depends on the non-parallelogram-likeness of grids. Biologically, the projection onto the first PC of  $\mathbf{f}(a; b_{train})$  can be realized by Hebbian learning of decoding weights [37], the nearest-centroid scheme can be realized by winner-take-all decision making [20], and the overlap of the mass centers in Decoder 2 can be realized by homeostatic mechanisms [38] to keep the mean neuronal activity over different iso- $b$  lines unchanged (**eq. S19**).

Consistently with the decoding scenario above, when decoding temporal flow generalizing across spatial information in the production epoch of t-SR, the error of Decoder 1 negatively correlated with the angle  $\theta$  between the first temporal-flow PC and the first spatial PC, and positively correlated with the portion  $\rho_{mix}$  of mixed variance (**Fig. 4c, d**); whereas the error of Decoder 2 depended weakly on  $\theta$ , and positively correlated with  $\rho_{mix}$  (**Fig. 4e, f**), see Methods for details. Thanks to the angle orthogonality and small mixed variance (**Fig. 3**), both decoders have above-chance performance (**Fig. 4g**). Additionally, for both t-SR and t-DM tasks, we studied the decoding generalization of temporal (non-temporal) information across non-temporal (temporal) information in all the perception, delay and production epochs. In all cases, we found how the decoding error depended on the angle between the first PCs of the decoded and generalized variables and the mixed variance followed similar scenario to above (**Figs. S7, S8**).

## Sequential activity and network structure

A common feature of the network dynamics in all the epochs of the four timing tasks above was neuronal sequential firing (**Fig. 5a** and **Fig. S9a-c**). We ordered the peak firing time of the neurons, and then measured the recurrent weight as a function of the order difference between two neurons. We found, on average, stronger connections from earlier- to later-peaking neurons than from later- to earlier-peaking neurons (**Fig. 5b** and **Fig. S9d-f**) [39, 40, 27]. To study the network structure that supported the coding orthogonality of temporal flow and non-temporal information in the perception and production epochs of t-SR (or t-DM), we classified the neurons into groups according to their preferred spatial location (or decision choice). Given a neuron  $i$  and a group  $\mathcal{G}$  of neurons ( $i$  may or may not belong to  $\mathcal{G}$ ), we ordered their peak times, and investigated the recurrent weight from  $i$  to each neuron of  $\mathcal{G}$  (except  $i$  itself if  $i \in \mathcal{G}$ ), see Methods for details. In this way, we studied the recurrent weight  $w(o_{post} - o_{pre}, |x_{post} - x_{pre}|)$  as a function of the difference  $o_{post} - o_{pre}$  between the peak orders of post- and pre-synaptic neurons and the difference  $|x_{post} - x_{pre}|$  of their preferred non-temporal information (**Fig. 5c, d**). In t-SR, firstly,  $w(o_{post} - o_{pre}, 0)$  exhibited similar asymmetry as that in IP (**Fig. 5b**), positive if  $o_{post} - o_{pre} > 0$  and negative if  $o_{post} - o_{pre} < 0$ , which drove sequential activity. Secondly,  $w(1, |x_{post} - x_{pre}|)$  decreased with  $|x_{post} - x_{pre}|$ , and became negative when  $|x_{post} - x_{pre}|$  was large enough (**Fig. 5c**). Together, the network of t-SR can be regarded as of several feedforward sequences, with two sequences exciting or inhibiting each other depending on whether their spatial preferences are similar or far different. The sequential activity coded the flow of time, and the short-range excitation and long-range inhibition maintained the spatial information [41]. Similar scenario also existed in the network of t-DM (**Fig. 5d**), where the sequential activity coded the flow of time, and the inhibition between the sequences of different decision preferences provided the mutual inhibition necessary for making decisions [42].

The scenario that feedforward structure hidden in recurrent connections drives sequential firing has been observed in a number of modeling works [39, 40, 27]. Our work extends this scenario to the interaction of multiple feedforward sequences, which can code temporal flow and non-temporal information simultaneously.

## Understanding the strong temporal signals in non-timing tasks

We have shown that in the perception and production epochs of t-SR and t-DM, when the network is required to record the temporal flow and maintain the non-temporal information simultaneously, neuronal temporal profiles exhibit similarity across non-temporal information (**Fig. 3b** and **Fig. S5a**) and the subspaces coding temporal flow and non-temporal information are orthogonal with small mixed variance (**Fig. 3d, e, i, j**). Interestingly, in tasks which do not require temporal information to perform, such profile similarity, orthogonality and small mixed variance were also experimentally observed [18, 19]. Moreover, the time-dependent variance explained more than 75% of the total variance in some non-timing tasks [18, 19]. It would be

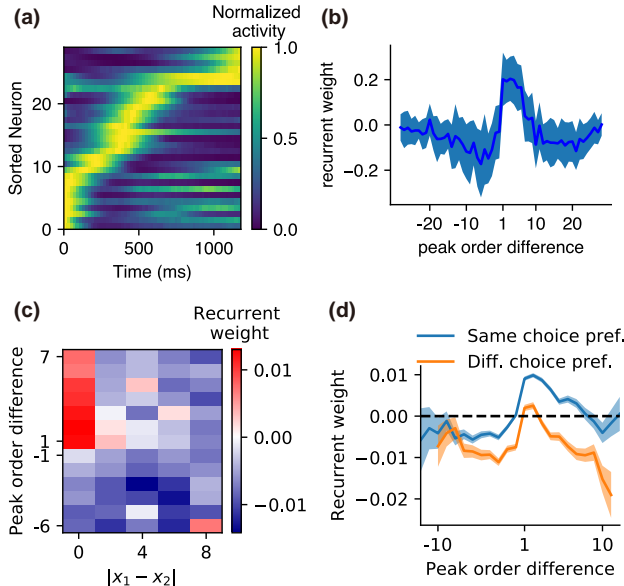


Figure 5: **Sequential activity and network structure.** (a) An example of neuronal activity (with maximum normalized to 1) in the perception epoch of IP task, sorted according to peak time. (b) Mean (solid line) and s.d. (shaded belt) of the recurrent weights as a function of the peak order difference between post- and pre-synaptic neurons in the perception epoch of IP. (c) Recurrent weight as a function of the difference  $|x_1 - x_2|$  between the preferred spatial locations of post- and pre-synaptic neurons and their peak order difference in the perception epoch of t-SR. (d) Recurrent weight as a function of peak order difference in the sequence of neurons with the same (blue) or different (orange) preferred decision choices in the perception epoch of t-DM. Shaded belt indicates s.e.m. See the sequential activity and network structure in other epochs of the four timing tasks of **Fig. 1b,c** in **Fig. S9**.

interesting to ask why non-timing tasks developed so strong temporal signals, thereby understanding the factors that facilitate the formation of time sense of animals.

First of all, before we studied the reasons for the strong temporal signals observed in non-timing tasks, we studied how the requirement of temporal processing influences the temporal signal strength. To this end, we studied spatial reproduction task (SR), where the network was to reproduce the spatial location immediately after a fixed delay (**Fig. 6a, left column, first row**), and decision making task (DM), where the network was to decide which stimulus was stronger immediately after the presentation of two stimuli (**Fig. 6a, right column, first row**). Unlike t-SR (or t-DM) (**Fig. 1c**), SR (or DM) did not require the network to record time between the two pulses (or during the presentation of the two stimuli). We used  $p_t = \text{Var}_{i,t}(\langle r_i(t,x) \rangle_x) / \text{Var}_{i,t,x}(r_i(t,x))$  to be the portion of time-dependent variance in the total variance  $\text{Var}_{i,t,x}(r_i(t,x))$ , with  $r_i(t,x)$  being the firing rate of the  $i$ th neuron at time  $t$  and non-temporal information  $x$ . We compared the portions  $p_t$ (t-SR) and  $p_t$ (t-DM) in the perception epochs of t-SR and t-DM with the portion  $p_t$ (SR) in the delay epoch of SR and that  $p_t$ (DM) during the presentation of stimuli in DM. We found that  $p_t$ (SR)  $<$   $p_t$ (t-SR) and  $p_t$ (DM)  $<$   $p_t$ (t-DM) (**Fig. 6b**). Therefore, temporal signals are stronger in timing tasks. However, even in the two timing tasks t-SR and t-DM we studied, the portion of time-dependent variance was smaller than the portion (75%) experimentally observed in non-timing tasks [18, 19] (**Fig. 6b**). Therefore, there should exist other factors than the timing requirement that are important to the formation of temporal signals.

Specifically, we studied the following four factors: (1) temporal complexity of task, (2) overlap of sensory input, (3) multi-tasking, and (4) timing anticipation.

*Temporal complexity of task.* Temporal complexity measures the complexity of spatio-temporal patterns that the network receives or outputs in a task [27]. To test the influence of temporal complexity on the strength of temporal signals, we designed comparison (COMP) and change detection (CD) tasks that enhanced the temporal complexity of SR and cue-dependent decision making (cue-DM) task that enhanced the temporal complexity of DM (**Fig. 6a**). In COMP, the network was to report whether the spatial coordinate of the stimulus presented before the delay was smaller or larger than that of the stimulus presented after the delay, in consistent with its vibrotactile version [18] (**Fig. 1d**). In CD, the network was to report whether the two stimuli presented before and after the delay were the same [21]. In cue-DM, the network was to report the index of the stronger or weaker stimulus, depending on the cue flashed at the end of the presented stimuli. COMP and CD have higher temporal complexity than SR because the output not only depends on the stimulus before the delay but also the stimulus after the delay. Similarly, cue-DM has higher temporal complexity than DM because the output also depends on the cue. We found that  $p_t$ (SR)  $<$   $p_t$ (CD),  $p_t$ (SR)  $<$   $p_t$ (COMP) and  $p_t$ (DM)  $<$   $p_t$ (cue-DM), suggesting that temporal complexity increases the portion of time-dependent variance (**Fig. 6c**). It has been empirically found that the task temporal complexity increases the temporal fluctuations in neuronal sequential firing [27]. Here we showed that the temporal fluctuation of the average neuronal activity  $\{\langle r_i(t,x) \rangle_x\}_i$  over non-timing information also increases with the temporal complexity of the task. The result  $p_t$ (SR)  $<$   $p_t$ (COMP) is consistent with the experimental observation that the population state varied more with time in COMP than in SR [20].

*Overlap of sensory input.* Suppose the population states of the sensory neurons in response to two stimuli  $x_1$  and  $x_2$  are respectively  $s_1$  and  $s_2$ . If  $s_1$  and  $s_2$  have high overlap, then the evolution trajectories of the recurrent network in response to  $x_1$  and  $x_2$  should be close to each other. In this case, the variance of the trajectories induced by the stimulus difference is small,

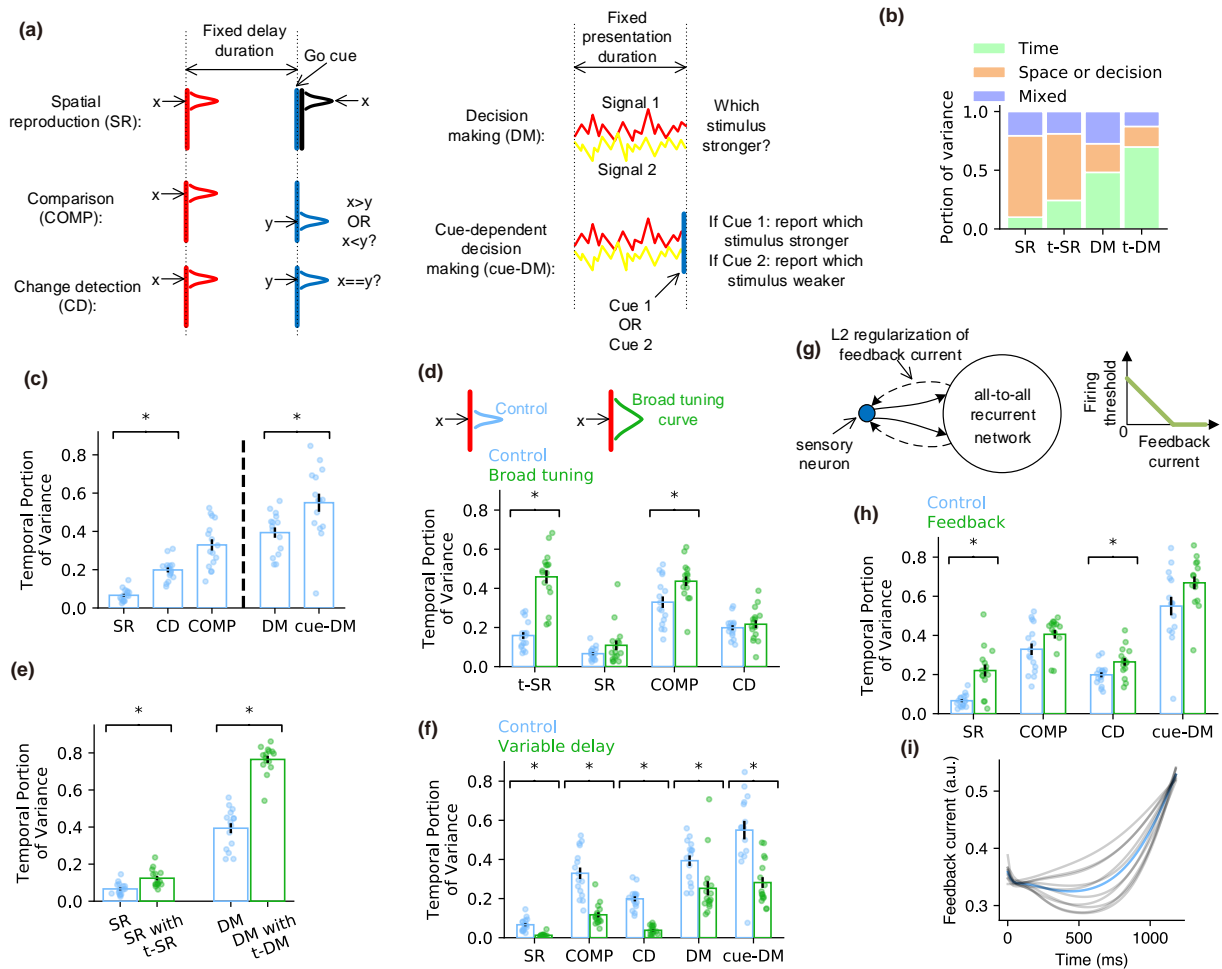


Figure 6: **Understanding the strong temporal signals in non-timing tasks.** (a) Schematic of the non-timing tasks we studied. (b) Bar charts show how the total signal variance is split among temporal information, non-temporal information and the residual variance unexplained by temporal and non-temporal information in SR, t-SR, DM and t-DM. (c) The portion of total variance explained by temporal signals in non-timing tasks. Error bars represent mean  $\pm$  s.e.m. across training configurations. Each dot corresponds to the value in a training configuration. Asterisk indicates significant difference at  $p < 0.05$  (two-sided Welch's t test). (d) The portion of time-dependent variance before (blue) and after (green) broadening the tuning curves of the sensory neurons. (e) The portion of time-dependent variance in SR or DM, when the network is trained on SR or DM only (blue), or trained on t-SR or t-DM concurrently (green). (f) The portion of time-dependent variance in fixed-delay (blue) or variable-delay (green) tasks. (g) Left: schematic of the feedback connections (dashed arrows) to the sensory neurons (blue dot) to study anticipatory attention. Solid arrows represent feedforward connections. Right: firing threshold of sensory neuron decreases with feedback current until zero. (h) The portion of time-dependent variance before (blue) and after (green) adding feedback to sensory neurons. (i) Feedback current as a function of time in the delay epoch of SR. Blue line: mean value. Gray lines: individual training configurations.

and the time-dependent variance explains a large portion of the total variance. To test this idea, we broadened the Gaussian tuning curves of the sensory neurons in t-SR, SR, COMP and CD tasks, and found increased portion of time-dependent variance (**Fig. 6d**).

*Multi-tasking.* The brain has been well trained on various timing tasks in everyday life, so the animal may also have a sense of time when performing non-timing tasks, which increases the time-dependent variance. To test this hypothesis, we trained networks on t-SR and SR concurrently, so that the network could perform either t-SR or SR indicated by an input signal. [26]. We also trained t-DM and DM concurrently. We only considered these two task pairs because the two tasks in each pair share the same number and type of inputs and outputs (except for a scalar Go-cue input in t-SR and t-DM), hence they do not require any changes in the network architecture. We found that both  $p_t(\text{SR})$  and  $p_t(\text{DM})$  were larger in networks that were also trained on timing tasks than in networks trained solely on non-timing tasks (**Fig. 6e**).

*Timing anticipation.* In the working memory experiments that observed strong time-dependent variance [18, 19], the delay period had fixed duration. This enabled the animals to learn this duration after long-term training and predict the end of the delay, thereby getting ready to take actions or receive new stimuli toward the end of the delay. If the delay period is variable, then the end of the delay will no longer be predictable. We found that the temporal signals in fixed-delay tasks were stronger than those in variable-delay tasks (**Fig. 6f**), which suggests that timing anticipation is a reason for strong temporal signals. A possible functional role of timing anticipation is anticipatory attention: a monkey might pay more attention to its finger or a visual location when a vibrotactile or visual cue was about to come toward the end of the delay to increase its sensitivity to the stimulus. To study the influence of this anticipatory attention to the formation of temporal signals, we supposed feedback connections from the recurrent network to the sensory neurons in our model (**Fig. 6g**). Feedback currents could reduce the firing thresholds of sensory neurons through disinhibition mechanism [43]. We also added L2 regularization on the feedback current (**Fig. 6g**) to reduce the energy cost of the brain (see Methods). After training, the feedback current stayed at a low level to reduce the energy cost, but became high when the cue was about to come to increase the sensitivity of the network (**Fig. 6i**). We found that adding this feedback mechanism increased the portion of time-dependent variance (**Fig. 6h**), because the feedback current, which increased with time toward the end of the delay (**Fig. 6i**), provided a time-dependent component of the population activity.

Collectively, other than the timing requirement in timing tasks, we identified four possible factors that facilitate the formation of strong temporal signals: (1) high temporal complexity of tasks; (2) large sensory overlap under different stimuli; (3) transfer of timing sense due to multi-tasking; (4) timing anticipation.

## Discussion

In summary, neural networks perceive time intervals through stereotypical dynamic trajectories, maintain time intervals by attractor dynamics in a complementary monotonic coding scheme, and perform interval production or comparison by scaling evolution speed. Temporal and non-temporal information are coded in orthogonal subspaces with small mixed variance, which facilitates decoding generalization. The network structure after training exhibits multiple feedforward sequences that mutually excite or inhibit depending on whether their preferences of non-temporal information are similar or not. We identified four possible factors that facilitate the formation of strong temporal signals in non-timing tasks: temporal complexity of task, overlap of sensory input, multi-tasking and timing anticipation.

## Perception and production of time intervals

In the perception epoch, the network evolved along a stereotypical trajectory after the first pulse (**Fig. 2b, c**). Consistently, some neurons in the prefrontal cortex and striatum prefer to peak their activities around specific time points after an event [44]. In the brain, such stereotypical trajectory may not only formed by neuronal activity state, but also synaptic state such as slow synaptic current or short-term plasticity. The temporal information coded by the evolution of synaptic state can be read out by the network activity in response to a stimulus [45, 28, 46].

We also studied the trajectory speed with time during the perception epoch. We found that after a transient period, the speed in IP task stayed around a constant value (**Fig. S2a**), the speed in IC and t-DM tasks increased with time (**Figs. S3c, S5c**), and the speed in t-SR task decreased with time (**Fig. S4b**). Therefore, we did not make any general conclusion on the trajectory speed when the network perceiving time intervals.

The temporal scaling when producing or comparing intervals has been observed in animal experiments [12, 31, 33]. A possible reason why temporal scaling exhibit in both the production epoch of IP and the stimulus2 epoch of IC (**Fig. 2l-o** and **Fig. S3i-n**) is that both epochs require the network to compare the currently elapsed time with the time interval maintained in working memory. In IC, the decision choice is switched as soon as the trajectory has passed the critical point at which the elapsed time  $t$  equals to the maintained interval  $T$ ; in IP, the network is required to output a movement as soon as  $t = T$ : both tasks share a decision-making process around the  $t = T$  time point. This temporal scaling enables generalizable decoding of the portion  $t/T$  of the elapsed time (**Figs. S7g, 8g**), which enables people to identify the same speech or music played at different speeds [47, 48].

When the to-be-produced interval  $T$  gets changed, the trajectory in the perception epoch is truncated or lengthened (**Fig. 2b-d**), whereas the trajectory in the production epoch is temporally scaled (**Fig. 2l-o**). This difference helps us to infer the psychological activity of the animal. For example, in the fixed-delay working memory task, when the delay period was changed, the neuronal activity during the delay was temporally scaled [18]. This implies that the animals had already learned the duration of the delay, and were actively using this knowledge to anticipate the coming stimulus, instead of passively perceiving time. However, this anticipation was not feasible before the animal had learned the delay duration. Therefore, we predict that at the beginning of training, the animal perceived time using stereotypical trajectory, and the scaling phenomenon gradually emerged during training.

## Combination of temporal and non-temporal information

Temporal and non-temporal information are coded orthogonally with small mixed variance (**Fig. 3**). Physically, time is consistently flowing, regardless of the non-temporal information; and much information is also invariant with time. The decoding generalizability resulted from this coding geometry (**Fig. 4**) helps the brain to develop a shared representation of time across non-temporal information or a shared representation of non-temporal information across time using a fixed set of readout weights. Decoding generalizability of non-temporal information across time has been studied in working memory tasks [20, 49], and has been considered as an advantage of working memory models in which information is maintained in stable, or a stable subspace of, neuronal activity [20, 50]. Here we showed that with this geometry, such advantage also exists for reading out temporal information.

Interestingly, the orthogonality and small mixed variance have been experimentally observed in non-timing tasks [18, 19], so their formation seems not to depend on the timing task requirement. Consistently, in the delay epoch of t-SR and t-DM, although the network needed not to record the temporal flow to perform the tasks, temporal flow and non-temporal information were still coded orthogonally with small mixed variance (**Fig. S10a-d**). By comparing the orthogonality and mixed variance in the perception epoch of t-SR and t-DM with those in the non-timing tasks (**Fig. 6a**), we found that timing task requirement did not influence the orthogonality, but generally reduced the mixed variance (**Fig. S10e, f**). The network structure in non-timing tasks also exhibited interacting feedforward sequences (**Fig. S10g-k**).

## Strong temporal signals in non-timing tasks

Our results concerning the various factors that affect the strength of temporal signals in non-timing tasks lead to testable experimental predictions. The result of sensory overlap (**Fig. 6d**) implies that sensory neurons with large receptive fields are essential to the strong temporal signals. The result of multi-tasking (**Fig. 6e**) implies that animals better trained on timing or music have stronger temporal signals when performing non-timing tasks. The result of temporal complexity (**Fig. 6c**) implies that animals have stronger temporal signals when performing tasks with higher temporal complexity, which is consistent with some experimental clues [20]. The result of timing anticipation (**Fig. 6f**), consistently with Ref. [27], implies that if the appearance of an event is unpredictable, then the temporal signals should be weakened. Besides anticipatory attention (**Fig. 6g**), anticipation may influence the temporal signals through other mechanisms. In the fixed-delay comparison task (**Fig. 1d**), suppose a stimulus  $a$  appeared before the delay, then both the population firing rate and the information about  $a$  in the population state increase toward the end of the delay period [51]. It is believed that this is because the information about  $a$  was stored in short-termly potentiated synapses in the middle of the delay to save the energetic cost of neuronal activity, while got retrieved into the population state near the end of the delay period to facilitate information manipulation [52]. This storing and retrieving process may also be a source of temporal signals.

## Interval and beat based timing

We have discussed the processing of single time intervals using our model. However, recent evidences imply that the brain may use different neural substrates and mechanisms to process regular beats from single time intervals [53, 54]. Dynamically, in the medial premotor cortices, different regular tapping tempos are coded by different radii of circular trajectories that travel at a constant speed [54], which is different from the stereotypical trajectory or speed scaling scenario revealed in our model (**Fig. 2b-d, l-o**). The distribution of the preferred intervals of the tapping-interval-tuned neurons is wide, peaking around 850 ms [55, 56], which is also different from the complementary monotonic tuning scenario in our model (**Fig. 2j, k**). Additionally, humans tend to use a counting scheme to estimate single time intervals when the interval duration is longer than 1200 ms [57], which implies that the beat-based scheme is mentally used to reduce the estimation error of single long intervals even without external regular beats. However, after we trained our network model to produce intervals up to 2400 ms, it processed intervals between 1200 ms and 2400 ms in similar schemes (**Fig. S11**) to that illustrated in **Fig. 2** for intervals below 1200 ms. All these results suggest the limitation of our model to explain beat-based timing. Modeling work on beat-based timing is the task of future research.

## Methods

Methods and Figs. S1 to S11 are provided in supplementary information. In the method section, we present the details of our computational model, including the network structure, the tasks to be performed and the methods we used to train the network model. We also present the details to analyze the interval-coding scheme in the delay and production epochs (**Fig. 2**), the coding combination of temporal and non-temporal information (**Figs. 3, 6b**), decoding generalization (**Fig. 4**) as well as the firing and structural sequences (**Fig. 5**). We also explain the relationship between the monotonic coding at the end of the delay epoch and the low dimensionality of the attractor (**Fig. 2g, k**), as well as the geometric meaning of mixed variance (**Fig. 3**) in supplementary information. Computer code is available from <https://github.com/zedongbi/IntervalTiming>.

## Acknowledgment

This work was supported by Hong Kong Baptist University (HKBU) Strategic Development Fund and HKBU Research Committee and Interdisciplinary Research Clusters Matching Scheme 2018/19 (RC-IRCMs/18-19/SCI01). This research was conducted using the resources of the High-Performance Computing Cluster Centre at HKBU, which receives funding from the RGC and HKBU.

## References

- [1] H. Merchant, D. L. Harrington, and W. H. Meck, “Neural basis of the perception and estimation of time,” *Annu. Rev. Neurosci.*, vol. 36, pp. 313–336, 2013.
- [2] M. J. Allman, S. Teki, T. D. Griffiths, and W. H. Meck, “Properties of the internal clock: First- and second-order principles of subjective time,” *Annu. Rev. Psychol.*, vol. 65, pp. 1–29, 2014.
- [3] J. J. Paton and D. V. Buonomano, “The neural basis of timing: Distributed mechanisms for diverse functions,” *Neuron*, vol. 98, pp. 687–705, 2018.
- [4] E. A. Petter, S. J. Gershman, and W. H. Meck, “Integrating models of interval timing and reinforcement learning,” *Trends Cogn. Sci.*, vol. 22, pp. 911–922, 2018.
- [5] M. D. Mauk and D. V. Buonomano, “The neural basis of temporal processing,” *Annu. Rev. Neurosci.*, vol. 27, p. 307, 2004.
- [6] C. V. Buhusi and W. H. Meck, “What makes us tick? Functional and neural mechanisms of interval timing,” *Nat. Rev. Neurosci.*, vol. 6, pp. 755–765, 2005.
- [7] M. Treisman, “Temporal discrimination and the indifference interval. Implications for a model of the “internal clock,”” *Psychol. Monogr.*, vol. 77, pp. 1–31, 1963.
- [8] P. R. Killeen and J. G. Fetterman, “A behavioral theory of timing,” *Psychol. Rev.*, vol. 95, pp. 274–295, 1988.
- [9] R. H. R. Hahnloser, A. A. Kozhevnikov, and M. S. Fee, “An ultra-sparse code underlies the generation of neural sequence in a songbird,” *Nature*, vol. 419, pp. 65–70, 2002.
- [10] G. F. Lynch, T. S. Okubo, A. Hanuschkin, R. H. R. Hahnloser, and M. S. Fee, “Rhythmic continuous-time coding in the songbird analog of vocal motor cortex,” *Neuron*, vol. 90, pp. 877–892, 2016.
- [11] M. S. Matell and W. H. Meck, “Cortico-striatal circuits and interval timing: coincidence detection of oscillatory processes,” *Brain Res. Cogn. Brain Res.*, vol. 21, pp. 139–170, 2004.
- [12] J. Wang, D. Narain, E. A. Hosseini, and M. Jazayeri, “Flexible timing by temporal scaling of cortical responses,” *Nat. Neurosci.*, vol. 21, pp. 102–110, 2018.
- [13] S. Teki and T. D. Griffiths, “Working memory for time intervals in auditory rhythmic sequences,” *Front. Psychol.*, vol. 5, p. 1329, 2014.
- [14] R. B. Ivry and J. E. Schlerf, “Dedicated and intrinsic models of time perception,” *Trends Cogn. Sci.*, vol. 12, pp. 273–280, 2008.
- [15] A. H. Lara and J. D. Wallis, “The role of prefrontal cortex in working memory: A mini review,” *Front. Syst. Neurosci.*, vol. 9, p. 173, 2015.
- [16] J. I. Gold and M. N. Shadlen, “The neural basis of decision making,” *Annu. Rev. Neurosci.*, vol. 30, pp. 535–574, 2007.
- [17] R. Romo, C. D. Brody, A. Hernandez, and L. Lemus, “Neuronal correlates of parametric working memory in the prefrontal cortex,” *Nature*, vol. 399, pp. 470–473, 1999.
- [18] C. K. Machens, R. Romo, and C. D. Brody, “Functional, but not anatomical, separation of “what” and “when” in prefrontal cortex,” *J. Neurosci.*, vol. 30, pp. 350–360, 2010.
- [19] D. Kobak, W. Brendel, C. Constantinidis, C. E. Feierstein, A. Kepecs, Z. F. Mainen, X.-L. Qi, R. Romo, N. Uchida, and C. K. Machens, “Demixed principal component analysis of neural population data,” *eLife*, vol. 5, p. e10989, 2016.
- [20] J. D. Murray, A. Bernacchia, N. A. Roy, C. Constantinidis, R. Romo, and X.-J. Wang, “Stable population coding for working memory coexists with heterogeneous neural dynamics in prefrontal cortex,” *Proc. Natl. Acad. Sci. USA*, vol. 114, pp. 394–399, 2017.
- [21] R. Rossi-Poola, J. Zizumbo, M. Alvarez, J. Vergara, A. Zainosa, and R. Romo, “Temporal signals underlying a cognitive process in the dorsal premotor cortex,” *Proc. Natl. Acad. Sci. USA*, vol. 116, pp. 7523–7532, 2019.
- [22] H. Hong, D. L. K. Yamins, N. J. Majaj, and J. J. DiCarlo, “Explicit information for category-orthogonal object properties increases along the ventral stream,” *Nat. Neurosci.*, vol. 19, pp. 613–622, 2016.
- [23] H. F. Song, G. R. Yang, and X.-J. Wang, “Training excitatory-inhibitory recurrent neural networks for cognitive tasks: A simple and flexible framework,” *PLoS Comp. Bio.*, vol. 12, p. e1004792, 2016.
- [24] V. Mante, D. Sussillo, K. V. Shenoy, and W. T. Newsome, “Context-dependent computation by recurrent dynamics in prefrontal cortex,” *Nature*, vol. 503, pp. 78–84, 2013.
- [25] D. Sussillo, M. M. Churchland, M. T. Kaufman, and K. V. Shenoy, “A neural network that finds a naturalistic solution for the production of muscle activity,” *Nat. Neurosci.*, vol. 18, pp. 1025–1033, 2015.
- [26] G. R. Yang, M. R. Joglekar, H. F. Song, W. T. Newsome, and X.-J. Wang, “Task representations in neural networks trained to perform many cognitive tasks,” *Nat. Neurosci.*, vol. 22, pp. 297–306, 2019.
- [27] A. E. Orhan and W. J. Ma, “A diverse range of factors affect the nature of neural representations underlying short-term memory,” *Nat. Neurosci.*, vol. 22, pp. 275–283, 2019.
- [28] U. R. Karmarkar and D. V. Buonomano, “Timing in the absence of clocks: Encoding time in neural network states,” *Neuron*, vol. 53, pp. 427–438, 2007.
- [29] H. S. Seung, “How the brain keeps the eyes still,” *Proc. Natl. Acad. Sci. USA*, vol. 93, pp. 13339–13344, 1996.
- [30] A. Mita, H. Mushiaki, K. Shima, Y. Matsuzaka, and J. Tanji, “Interval time coding by neurons in the presupplementary and supplementary motor areas,” *Nat. Neurosci.*, vol. 12, p. 502, 2009.

- [31] E. D. Remington, D. Narain, E. A. Hosseini, and M. Jazayeri, “Flexible sensorimotor computations through rapid reconfiguration of cortical dynamics,” *Neuron*, vol. 98, pp. 1005–1019, 2018.
- [32] M. I. Leon and M. N. Shadlen, “Representation of time by neurons in the posterior parietal cortex of the macaque,” *Neuron*, vol. 38, p. 317, 2003.
- [33] G. Mendoza, J. C. Méndez, O. Pérez, L. Prado, and H. Merchant, “Neural basis for categorical boundaries in the primate pre-SMA during relative categorization of time intervals,” *Nat. Commun.*, vol. 9, p. 1098, 2018.
- [34] J. Ashe and A. P. Georgopoulos, “Movement parameters and neural activity in motor cortex and area 5,” *Cereb. Cortex*, vol. 4, p. 590, 1994.
- [35] M. M. Churchland, J. P. Cunningham, M. T. Kaufman, J. D. Foster, P. Nuyujukian, S. I. Ryu, and K. V. Shenoy, “Neural population dynamics during reaching,” *Nature*, vol. 487, p. 51, 2012.
- [36] M. Lankarany, D. Al-Basha, S. Ratté, and S. A. Prescott, “Differentially synchronized spiking enables multiplexed neural coding,” *Proc. Natl. Acad. Sci. USA*, vol. 116, p. 10097, 2019.
- [37] P. Dayan and L. F. Abbott, *Theoretical neuroscience: computational and mathematical modeling of neural systems*. Cambridge: The MIT Press, 2001.
- [38] G. Turrigiano, “Too many cooks? Intrinsic and synaptic homeostatic mechanisms in cortical circuit refinement,” *Annu. Rev. Neurosci.*, vol. 34, pp. 89–103, 2011.
- [39] K. Rajan, C. D. Harvey, and D. W. Tank, “Recurrent network models of sequence generation and memory,” *Neuron*, vol. 90, pp. 128–142, 2016.
- [40] N. F. Hardy and D. V. Buonomano, “Encoding time in feedforward trajectories of a recurrent neural network model,” *Neural Comput.*, vol. 30, pp. 378–396, 2018.
- [41] S. Lim and M. S. Goldman, “Balanced cortical microcircuitry for spatial working memory based on corrective feedback control,” *J. Neurosci.*, vol. 34, pp. 6790–6806, 2014.
- [42] X.-J. Wang, “Probabilistic decision making by slow reverberation in cortical circuits,” *Neuron*, vol. 36, pp. 955–968, 2002.
- [43] R. Hattori, K. V. Kuchibhotla, R. C. Froemke, and T. Komiyama, “Functions and dysfunctions of neocortical inhibitory neuron subtypes,” *Nat. Neurosci.*, vol. 20, pp. 1199–1208, 2017.
- [44] D. Z. Jin, N. Fujii, and A. M. Graybiel, “Neural representation of time in cortico-basal ganglia circuits,” *Proc. Natl. Acad. Sci. USA*, vol. 106, pp. 19156–19161, 2009.
- [45] D. V. Buonomano, “Decoding temporal information: A model based on short-term synaptic plasticity,” *J. Neurosci.*, vol. 106, pp. 1129–1141, 2000.
- [46] O. Pérez and H. Merchant, “The synaptic properties of cells define the hallmarks of interval timing in a recurrent neural network,” *J. Neurosci.*, vol. 38, pp. 4186–4199, 2018.
- [47] R. Güttig and H. Sompolinsky, “Time-warp-invariant neuronal processing,” *PLoS Biol.*, vol. 7, p. e1000141, 2009.
- [48] V. Goudar and D. V. Buonomano, “Encoding sensory and motor patterns as time-invariant trajectories in recurrent neural networks,” *eLife*, vol. 7, p. e31134, 2018.
- [49] M. G. Stokes, M. Kusunoki, N. Sigala, H. Nili, D. Gaffan, and J. Duncan, “Dynamic coding for cognitive control in prefrontal cortex,” *Neuron*, vol. 78, pp. 364–375, 2013.
- [50] S. Druckmann and D. B. Chklovskii, “Neuronal circuits underlying persistent representations despite time varying activity,” *Curr. Biol.*, vol. 22, pp. 2095–2103, 2012.
- [51] O. Barak, M. Tsodyks, and R. Romo, “Neuronal population coding of parametric working memory,” *J. Neurosci.*, vol. 30, pp. 9424–9430, 2010.
- [52] N. Y. Masse, G. R. Yang, H. F. Song, X.-J. Wang, and D. J. Freedman, “Circuit mechanisms for the maintenance and manipulation of information in working memory,” *Nat. Neurosci.*, vol. 22, pp. 1159–1167, 2019.
- [53] S. Teki, M. Grube, S. Kumar, and T. D. Griffiths, “Distinct neural substrates of duration-based and beat-based auditory timing,” *J. Neurosci.*, vol. 31, pp. 3805–3812, 2011.
- [54] J. Gámez, G. Mendoza, L. Prado, A. Betancourt, and H. Merchant, “The amplitude in periodic neural state trajectories underlies the tempo of rhythmic tapping,” *PLoS Biol.*, vol. 17, p. 4, 2019.
- [55] H. Merchant, O. Pérez, W. Zarco, and J. Gámez, “Interval tuning in the primate medial premotor cortex as a general timing mechanism,” *J. Neurosci.*, vol. 33, pp. 9082–9096, 2013.
- [56] R. Bartolo, L. Prado, and H. Merchant, “Information processing in the primate basal ganglia during sensory-guided and internally driven rhythmic tapping,” *J. Neurosci.*, vol. 34, pp. 3910–3923, 2014.
- [57] S. Grondin, G. Meilleur-Wells, and R. Lachance, “When to start explicit counting in a time-intervals discrimination task: A critical point in the timing process of humans,” *J. Exp. Psychol. Hum. Percept. Perform.*, vol. 25, pp. 993–1004, 1999.

# Supplementary Information: Understanding the computation of time using neural network models

Zedong Bi, Changsong Zhou

November 20, 2021

## S1 Method

### S1.1 Network details

We adopted a discrete-time formulation of network dynamics, in which

$$\mathbf{x}_t = \mathbf{W}^{rec} \mathbf{r}_{t-1} + \mathbf{W}^{in} \mathbf{u}_t + \mathbf{W}^{in,att} [\mathbf{u}_t^{att} - \theta^{att}]_+ + \mathbf{b} + \sqrt{2\sigma_{rec}^2} \mathbf{N}(0, 1), \quad (\text{S1})$$

where  $\mathbf{x}_t$ ,  $\mathbf{r}_t$  and  $\mathbf{u}_t$  are respectively the synaptic current, firing rate and network input at time step  $t$ ,  $\mathbf{b}$  is the background input,  $\mathbf{W}^{rec}$  is the recurrent weight,  $\mathbf{W}^{in}$  is the input weight, and  $\sigma_{rec}$  is the strength of recurrent noise. We supposed  $\mathbf{u}_t = f(\mathbf{x}_t)$ , with  $f(\cdot)$  being the softplus current-rate transfer function, i. e.

$$f(x) = \log(1 + \exp(x)). \quad (\text{S2})$$

Input  $\mathbf{u}_t$  is also noisy,

$$\mathbf{u}_t = \mathbf{u}_{signal} + \sqrt{2\sigma_{in}^2} \mathbf{N}(0, 1), \quad (\text{S3})$$

with  $\sigma_{in}$  being the strength of input noise.  $\mathbf{W}^{in,att}$ ,  $\mathbf{u}_t^{att}$  and  $\theta^{att}$  are the quantities related to the input units modulated by top-down attention. They are only valid when studying the effect of anticipatory attention in non-timing tasks (**Fig. 6g-i**). The model does not have these quantities in the other tasks.  $\mathbf{W}^{in,att}$  is the weight from the attention-modulated units to the recurrent network,  $\mathbf{u}_t^{att}$  is the input current to the attention-modulated units, and  $\theta^{att}$  is the firing threshold of these units. The firing threshold is

$$\theta^{att} = [\theta_0^{att} - \mathbf{W}^{fb,att} \mathbf{r}_t]_+, \quad (\text{S4})$$

with  $\mathbf{W}^{fb,att}$  being positive feedback weight, so that  $\theta^{att}$  decreases with feedback current until to zero, starting from  $\theta_0^{att} = 1.5$ . Eq. S4 models the disinhibitory effect of feedback connections [1]. Similar to  $\mathbf{u}_t$ ,  $\mathbf{u}_t^{att}$  is also noisy, with the noise strength  $\sigma_{in}^2$  (eq. S3).

Some previous studies started with a continuous-time formulation, and obtained the discrete-time version using Euler method (omitting the attention-modulated units):

$$\mathbf{x}_t = (1 - \alpha) \mathbf{x}_{t-1} + \alpha (\mathbf{W}^{rec} \mathbf{r}_{t-1} + \mathbf{W}^{in} \mathbf{u}_t + \mathbf{b} + \sqrt{2\alpha^{-1}\sigma_{rec}^2} \mathbf{N}(0, 1)), \quad (\text{S5})$$

with  $\alpha = \Delta t / \tau$  being the ratio of time step length  $\Delta t$  and membrane time constant  $\tau$ . In our study, we effectively set  $\alpha = 1$ , similarly as the scheme used in Ref. [2, 3]. We also set  $\Delta t = 20$  ms. The output of the network is supposed to be

$$z = \mathbf{W}^{out} \mathbf{r} + \mathbf{b}^{out}, \quad (\text{S6})$$

with the dimension of  $z$  depending on tasks.

We set  $\sigma_{in} = 0.01$ ,  $\sigma_{rec} = 0.05$  when training the network. After training, when plotting the neuronal activities in the perception epoch (**Fig. 2b-d**), we kept  $\sigma_{in} = 0.01$ ,  $\sigma_{rec} = 0.05$  so that the neuronal temporal profiles under different durations of perception epoch did not fully overlap. When doing the other analysis, we turned off the noises by default.

### S1.2 Task details

#### S1.2.1 Timing tasks

*Interval production task (IP)*. The network received from 2 input units: from one came the two pulses that defined the time interval, and from the other came the Go cue. The interval between the beginning of the simulation and the onset of the first pulse was

$$T_{start} \sim U(60 \text{ ms}, 500 \text{ ms}), \quad (\text{S7})$$

where  $U(t_1, t_2)$  is a uniform distribution between  $t_1$  and  $t_2$ . The interval between the offset of the first pulse and the onset of the second pulse was

$$T \sim U(400 \text{ ms}, 1400 \text{ ms}). \quad (\text{S8})$$

Note that we set the range of  $T$  to be [400 ms, 1400 ms] during training, but after training, we only investigated the performance of the network when  $T \in [600 \text{ ms}, 1200 \text{ ms}]$ . The reason is that there were boundary effects if, after training,  $T$  took a value close to 400 ms or 1400 ms: if  $T$  was close to 400 ms, then the time interval produced by the network was biased to be larger than  $T$ ; whereas if  $T$  was close to 1400 ms, then the produced interval was biased to be smaller than  $T$ . Such biases were weak if  $T$  took a middle value (**Fig. S1e**).

The interval between the offset of the second pulse and the onset of the Go cue (i. e. , the delay period) was

$$T_{delay} \sim U(600 \text{ ms}, 1600 \text{ ms}). \quad (\text{S9})$$

All input pulses (including the two pulses that defined the time interval, and the Go cue) lasted for 60 ms, and had strength 1. Input units stayed at 0 when there were no pulses.

The target output was a scalar. It stayed at zero from the beginning, jumped to 1 at time  $T$  after the offset of the Go cue, and kept at 1 until the end of the simulation at 300ms afterwards.

*Interval comparison task (IC)*. The network received two successive long-lasting stimuli respectively from two input units. The first stimuli, which came from the first unit, started at time  $T_{start}$  after the beginning of the simulation, and lasted for duration  $T_1$ . Then after a delay interval  $T_{delay}$ , the second stimuli, which came from the second unit, started, and lasted for duration  $T_2$ .

$$T_{start} \sim U(60 \text{ ms}, 500 \text{ ms}), \quad T_1 \sim U(400 \text{ ms}, 1400 \text{ ms}), \quad T_{delay} \sim U(600 \text{ ms}, 1600 \text{ ms}), \quad T_2 \sim U(400 \text{ ms}, 1400 \text{ ms}) \quad (\text{S10})$$

All the input stimuli had strength 1. Input units stayed at 0 when there were no stimuli.

The target outputs were two scalars  $\hat{z}_0$  and  $\hat{z}_1$ . Both stayed at zero from the beginning. If  $T_1 > T_2$ , then  $\hat{z}_0$  jumped to 1 at the offset of the second stimulus, and stayed at 1 until the end of the simulation at 300 ms afterwards. Otherwise,  $\hat{z}_1$  jumped to 1 at the offset of the second stimulus.

*Timed spatial reproduction task (t-SR)*. The network successively received three pulses from three input channels. The first channel was a line that coded spatial locations. This line contained 32 units, whose preferred directions were uniformly spaced from -6 to 25. For unit  $i$  with preferred location  $y_i$ , its activity in a pulse with location  $x$  was

$$A_{in}(t) \exp\left[-\frac{1}{2}\left(\frac{|y_i - x|}{2}\right)^2\right], \quad (\text{S11})$$

where  $A_{in}(t) = 1$  during the presentation of the pulse and  $A_{in}(t) = 0$  at the other time. In our simulation, the spatial locations of the stimuli were uniformly drawn from 0 to 19. The second and third channels were both scalar inputs. The pulse from the second channel defined the time interval to be remembered together with the pulse from the first channel. The pulse from the third channel acted as Go cue.  $T_{start}$ ,  $T$  and  $T_{delay}$  were distributed similarly as in IP (eqs. S7-S9).

The target output was a line with 32 units, which represented response location using similar tuning curves as the ones used for the input line (eq. S11):

$$\hat{z}_i = A_{out}(t) \exp\left[-\frac{1}{2}\left(\frac{|y_i - x|}{2}\right)^2\right], \quad (\text{S12})$$

where the amplitude  $A_{out}(t)$  stayed at zero from the beginning, jumped to 1 at time  $T$  after the offset of the Go cue, and stayed at 1 until the end of the simulation at 300 ms afterwards.

*Timed decision making task (t-DM)*. The network received from three channels of scalar inputs. From the first two channels came the stimuli whose strengths were to be compared with each other, and from the last channel came the Go cue pulse. Starting from the beginning of simulation, the first two channels were set to 0 for duration  $T_{start}$ , and then jumped to  $A_1$  and  $A_2$  respectively; after  $T$  time, these two channels were set to 0 again. The Go cue pulse came at time  $T_{delay}$  after the offset of the first two channels. Here,

$$A_1 = \gamma + c, \quad A_2 = \gamma - c, \quad (\text{S13})$$

where  $\gamma$  was the average strength of these two stimuli and was distributed as  $\gamma \sim U(0.8, 1.2)$ , and  $c$  measured the strength difference of these two stimuli, and was distributed as

$$c \sim U(\{-0.08, -0.04, -0.02, -0.01, 0.01, 0.02, 0.04, 0.08\}), \quad (\text{S14})$$

where  $U(\{a_1, a_2, \dots, a_n\})$  denotes a discrete uniform distribution over the set  $\{a_1, a_2, \dots, a_n\}$ .  $T_{start}$ ,  $T$  and  $T_{delay}$  were distributed similarly as in interval production task (eqs. S7-S9).

The target outputs were two scalars  $\hat{z}_0$  and  $\hat{z}_1$ . Both stayed at zero from the beginning. If  $c > 0$ , then  $\hat{z}_0$  jumped to 1 at time  $T$  after the offset of the Go cue, and stayed at 1 until the end of the simulation at 300ms afterwards. Otherwise,  $\hat{z}_1$  jumped to 1 at time  $T$  after the offset of the Go cue.

### S1.2.2 Non-timing tasks: default settings

*Spatial reproduction task (SR)*. The network received pulses from two input channels. The first channel was a line that contained 32 units, coding spatial locations in the range  $[-6, 25]$  in the way indicated by eq. S11. In our simulation, the spatial locations of the stimuli were uniformly drawn from 0 to 19. The second channel is a scalar input. The duration  $T_{delay}$

of the delay epoch between the first and second pulses was 1200 ms. The target output was a line of 32 units (eq. S12), which was to indicate the location of the first pulse immediately after the second pulse.

*Comparison task (COMP)*. The network received pulses from two input channels, both of which were lines that contained 32 units successively gave two pulses to the network. The target outputs were two scalars  $\hat{z}_0$  and  $\hat{z}_1$ , which were to indicate whether or not the spatial coordinate of the first pulse was larger than that of the second pulse.

*Change detection task (CD)*. The network had the same structure as that in COMP. Two scalar outputs were to indicate whether or not the distance between the spatial locations of the two input pulses was within 1.

*Decision making task (DM)*. The network received from two channels of stimuli lasting for  $T = 1200$  ms. The two scalar outputs were to indicate which stimulus was stronger immediately after the ending of the two stimuli.

*Cue-dependent decision making task (cue-DM)*. The network received from two channels of stimuli lasting for  $T = 1200$  ms. At the 1140 ms after the presentation of the two stimuli, a two dimensional one-hot vector lasting for 60ms was input from a third channel. Two scalar outputs were to indicate the index of the stronger stimulus or the index of the weaker stimulus according to the third channel.

### S1.2.3 Non-timing tasks: studying the factors that influence the strength of temporal signal

To study the effect of the overlap of sensory input to the strength of temporal signal in the delay epoch of SR, COMP and CD (**Fig. 6d**), we expanded the unit number in the line channels to 44 (default is 32), and broadened the standard deviation of the tuning curves (eq. S12) to 4 (default is 2). These units coded spatial locations in the range -12 to 31. In our simulation, the spatial locations of input stimuli were uniformly drawn from 0 to 19.

To study the effect of multi-tasking (**Fig. 6e**), we trained the network on t-SR and SR concurrently, or on t-DM and DM concurrently. The two tasks in each pair share the same input and output channels. We used a one-hot vector from another two-dimensional input channel to indicate which task should be performed [4]. The network was to be able to perform either of the indicated task.

To study the effect of timing anticipation (**Fig. 6f**), we trained the network to perform SR, COMP, CD, DM and cue-DM, with the duration  $T$  of the delay epoch (for SR, COMP and CD) or the stimuli-presentation epoch (for DM and cue-DM) was randomly between [800 ms, 1600 ms]. After training, we analyzed the simulation results when  $T = 1200$  ms, and compared the results with the cases after training the network with  $T$  fixed at 1200 ms. To study the effect of anticipatory attention (**Fig. 6g-i**), feedback was imposed on the second input channel of SR, COMP and CD, and was imposed on the third channel of cue-DM. This means that these input channels were modeled using the third term at the right-hand side in eq. S1, instead of the second term.

## S1.3 Training details

Training was performed to minimize a cost function using back-propagation through time. Cost function was defined as

$$C = \sum_i m_i (z_i - \hat{z}_i)^2, \quad (\text{S15})$$

where  $i$  is the index of output units,  $z_i$  is the actual output defined by eq. S6,  $\hat{z}_i$  is the target output, and  $m_i$  is the mask. In all tasks,  $m_i = 0$  before the onset of the first stimulus, and  $m_i = 1$  afterwards; therefore, only the output after the onset of the first stimulus was constrained. When studying the effect of anticipatory attention in non-timing tasks (**Fig. 6g-i**), we added L2 regularization to feedback current  $\mathbf{I}^{fb} = \mathbf{W}^{fb,att} \mathbf{r}_t$  (see eq. S4), so that eq.S15 becomes  $C = \sum_i m_i (z_i - \hat{z}_i)^2 + \beta_{fb} \frac{1}{N_{i,t}} \sum_{i,t} (I_{i,t}^{fb})^2$ , with  $\beta_{fb} = 10^{-4}$ . This cost function was minimized using Adam optimizer at learning rate 0.0005, with batch size 64 in each training step. We trained 16 configurations to perform IP and IC tasks, and trained 30 configurations to perform t-SR and t-DM tasks. Different configurations were initialized using different random seeds.

Before training, recurrent self-connections ( $W_{ii}^{rec}$  in eq. S5) were initialized to 1, and other recurrent connections were initialized as independent Gaussian variables with mean 0 and standard deviation  $0.3/\sqrt{N_{rec}}$ , with  $N_{rec} = 256$  being the number of recurrent units. This initialization strategy was used in Ref. [3]. The identity self-connections prevent vanishing gradient during training [5], and the non-zero off-diagonal recurrent connections induce sequential activity in the network after training [3], so that the dynamics of the network becomes comparable to experimental observations [6, 7, 8, 9, 10]. Output connections were initialized as independent Gaussian variable with mean 0 and standard deviation  $1/\sqrt{N_{rec}}$ . Input connections from the line input were initialized as variables drawn uniformly from  $[-1/\sqrt{2\sigma_{tuning}}, 1/\sqrt{2\sigma_{tuning}}]$ , with  $\sigma_{tuning}$  being the standard deviation of the Gaussian tuning curve (eq. S11), which was 2 by default and 4 when studying the effect of input overlap in non-timing tasks. The input connections from the other channels were initialized as variables drawn uniformly from  $[-1/\sqrt{D_{channel}}, 1/\sqrt{D_{channel}}]$ , with  $D_{channel}$  being the dimension of the input channel.

Every 200 training steps, we evaluated the performance of the network using a batch of size 512, and stopped training as soon as the performance of the network reached criterion (**Fig. S1i-1**). We introduced our criterion in t-SR and t-DM in details, the other tasks shared similar criterion:

In t-SR, a time interval was considered to be produced if: (1) the activities of all the 32 output units were below 0.2 before the offset of the Go cue, (2) one of them went above 0.5 at some point  $t_p$  before  $T + 300$ ms after the offset time  $t_{off}^{cue}$  of the Go cue. The produced interval was  $T_p = t_{off}^{cue} - t_p$ . Output location at time  $t_p$  was read out using a population vector method (see the computer code in Ref. [4]). Training was stopped as soon as (1) time intervals were produced in over 95%

simulation trials, (2) the relative error of the produced intervals  $|T_p - T|/T < 0.025$ , (3) the output locations were on average within 0.8 of the input locations.

In t-DM, a time interval was considered to be produced if: (1) the activities of both output units  $z_0$  and  $z_1$  were below 0.2 before the offset of the Go cue, (2) one of them went above 0.5 at some time point  $t_p$  before  $T + 300$ ms after the offset  $t_{off}^{cue}$  of the Go cue, whereas the other one stayed below 0.5. The produced interval was  $T_p = t_{off}^{cue} - t_p$ . In the trials in which a time interval was produced, the decision was considered to be correct if: when  $c > 0$  (or  $c < 0$ ),  $z_0$  (or  $z_1$ ) went above 0.5 and  $z_1$  (or  $z_0$ ) kept below 0.5. Training was stopped as soon as (1) time intervals were produced in over 96% of simulation trials, (2) the relative error of the produced intervals  $|T_p - T|/T < 0.025$ , (3) the decision error rate was smaller than 0.02.

## S1.4 Data analysis

### S1.4.1 Types of neurons at the end of the delay epoch

In IP or IC, we supposed  $f_i(T)$  to be the activity of the  $i$ th neuron at the end of the delay epoch as a function of the duration  $T$  of the perception (for IP) or stimulus1 (for IC) epoch. We picked neurons that can be strongly activated at the end of the delay epoch, namely the neurons whose  $\max_{T \in [T_{min}, T_{max}]} f_i(T) > \theta_{sa}$ , with  $T_{min} = 600$  ms and  $T_{max} = 1200$  ms respectively being the minimal and maximal values of  $T$  in our simulation, and  $\theta_{sa} = 2$ . Our results are not sensitive to the value of  $\theta_{sa}$ . We classified  $f_i(T)$  of the picked neurons into three types, namely monotonically increasing (MoI), monotonically decreasing (MoD), and non-monotonic (non-M) in the following way: We divided the range of  $T$  (i.e.,  $[T_{min}, T_{max}]$ ) into four parts of the same length, and calculated the mean value of  $f_i(T)$  in these four parts, say  $f_i(\text{part } 1) = \frac{4}{T_{max} - T_{min}} \int_{T_{min}}^{T_{min} + (T_{max} - T_{min})/4} f_i(T) dT$ ,  $f_i(\text{part } 2) = \frac{4}{T_{max} - T_{min}} \int_{T_{min} + (T_{max} - T_{min})/4}^{T_{min} + 2(T_{max} - T_{min})/4} f_i(T) dT$ , etc. If  $f_i(\text{part } 1) \leq f_i(\text{part } 2) \leq f_i(\text{part } 3) \leq f_i(\text{part } 4)$ , then neuron  $i$  belongs to MoI type; if  $f_i(\text{part } 1) \geq f_i(\text{part } 2) \geq f_i(\text{part } 3) \geq f_i(\text{part } 4)$ , then neuron  $i$  belongs to MoD type; otherwise, neuron  $i$  belongs to non-M type.

In t-SR, we supposed  $g_i(T, x)$  to be the activity of the  $i$ th neuron at the end of the delay epoch as a function of  $T$  at a given location  $x$  of the first pulse. We picked neurons that can be strongly activated at the end of the delay epoch (i.e., the neurons whose  $\max_{\{T, x\}} g_i(T, x) > \theta_{sa}$ ). We then defined  $f_i(T) = \max_x g_i(T, x)$ , and classified neuron  $i$  into MoI, MoD or non-M types according to the monotonicity of  $f_i(T)$  in the similar way to the IP or IC case introduced above. Similarly, in t-DM, we classified neurons according to  $f_i(T) = \max_c g_i(T, c)$ , where  $c$  is the half difference between the strengths of the presented stimuli (eq. S13).

### S1.4.2 Temporal scaling in the production epoch

Analysis of temporal scaling was performed using similar technique to Ref. [2]. Specifically, we calculated the  $k$ th scaling component  $\mathbf{u}_{SC,k}$  through the following equation:

$$\mathbf{u}_{SC,k} = \arg \min_{\mathbf{u}} \frac{\sum_t \sum_T (\mathbf{r}_k^S(t; T) \mathbf{u} - \text{Mean}_T(\mathbf{r}_k^S(t; T) \mathbf{u}))^2}{\sum_t \sum_T (\mathbf{r}_k^S(t; T) \mathbf{u} - \text{Mean}_{\{t, T\}}(\mathbf{r}_k^S(t; T) \mathbf{u}))^2}, \quad (\text{S16})$$

where  $\mathbf{r}_k^S(t; T)$  is population activity at the scaled time when the duration of the perception epoch is  $T$  (see below for details), the denominator is the total variance of the trajectories, and the numerator is the variance that cannot be explained by temporal scaling. To calculate the first scaling component  $\mathbf{u}_{SC,1}$ , we set  $\mathbf{r}_1^S(t; T) = \mathbf{r}^{PC}(tT_p; T)$ , with  $0 \leq t \leq 1$ , where  $\mathbf{r}^{PC}$  is the projection of the population activity in the subspace spanned by the first 9 principal components, and  $T_p$  is the interval produced by the network in the production epoch; then we minimized  $\mathbf{u}$  in eq. S16. To calculate the second scaling component  $\mathbf{u}_{SC,2}$ , we set  $\mathbf{r}_2^S(t; T) = \mathbf{r}_1^S(t; T) - \mathbf{r}_1^S(t; T) \mathbf{u}_{SC,1}$ , and then minimized  $\mathbf{u}$  in eq. S16 in the subspace orthogonal to  $\mathbf{u}_{SC,1}$ . In this way, we calculated all the 9 scaling components one by one.

Scaling index (SI) of a subspace  $U$  was defined as

$$\text{SI} = \frac{\sum_t \sum_T (\mathbf{r}_1^S(t; T) U - \text{Mean}_T(\mathbf{r}_1^S(t; T) U))^2}{\sum_t \sum_T (\mathbf{r}_1^S(t; T) U - \text{Mean}_{\{t, T\}}(\mathbf{r}_1^S(t; T) U))^2}, \quad (\text{S17})$$

where  $\mathbf{r}_1^S(t; T) U$  is the projection of the scaled trajectory to the subspace  $U$ .

### S1.4.3 The geometry of coding combination

During the perception epoch of t-SR, the network state is quantified by the time elapsed from the beginning of the epoch (temporal flow) and the spatial information of the first pulse. At the end of the delay epoch of t-SR, the network state is quantified by the time interval between the first two pulses and the spatial information of the first pulse. During the production epoch of t-SR, the network state is quantified by temporal flow, time interval and spatial information. Similar scenario also exists in t-DM, except that the non-temporal information is the decision choice made by the network. In t-DM, the decision choice  $d$  depends on the sign of the half difference  $c$  between the strength of the presented two stimuli (eq. S13), we defined  $r_i(d = 1, \{a\}) = \langle r_i(c, \{a\}) \rangle_{c > 0}$  and  $r_i(d = -1, \{a\}) = \langle r_i(c, \{a\}) \rangle_{c < 0}$ , where  $\{a\}$  indicates the other parameters than decision choice, and used  $r_i(d, \{a\})$  to do the following analysis. Together, during the perception epoch and at the end of the delay epoch of t-SR and t-DM, two variables are coded in the network state; during the production epoch, three variables are coded in the network state. We used two measurements to quantify the geometry of the coding combination of

multiple variables: (1) the angle between the first marginal principal components and (2) the mixed variance [11], introduced below.

Suppose the activity of the  $i$ th neuron  $r_i(a, b)$  is a function of two variables  $a$  and  $b$ , with the mean of  $r_i(a, b)$  being subtracted so that  $\langle r_i(a, b) \rangle_{a,b} = 0$ . The marginal principal components (PCs) with respect to  $a$  are the PCs of the dot set  $\{\langle r_i(a, b) \rangle_b\}_i$ , and the marginal PCs of  $b$  are the PCs of  $\{\langle r_i(a, b) \rangle_a\}_i$ . We quantified the coding orthogonality of  $a$  and  $b$  by calculating the angle between the first marginal PCs of  $a$  and  $b$ . The portions of variance explained by  $a$  and  $b$  are respectively  $p_a = \text{Var}_{i,a}(\{\langle r_i(a, b) \rangle_b\}_i)/v_{tot}$  and  $p_b = \text{Var}_{i,b}(\{\langle r_i(a, b) \rangle_a\}_i)/v_{tot}$ , with the total variance  $v_{tot} = \text{Var}_{i,a,b}(\{r_i(a, b)\}_i)$ . The portion of mixed variance between  $a$  and  $b$  is  $p_{a+b} = 1 - p_a - p_b$ .

In the case that the activity of the  $i$ th neuron  $r_i(a, b, c)$  is a function of three variables, we also subtracted the mean of  $r_i(a, b, c)$  so that  $\langle r_i(a, b, c) \rangle_{a,b,c} = 0$ . The marginal PCs of  $a$ ,  $b$  and  $c$  are respectively the PCs of  $\{\langle r_i(a, b, c) \rangle_{b,c}\}_i$ ,  $\{\langle r_i(a, b, c) \rangle_{a,c}\}_i$  and  $\{\langle r_i(a, b, c) \rangle_{a,b}\}_i$ . The portions of variance explained by these variables and their mixing were defined as [11]:

$$\begin{aligned} p_a &= \text{Var}_{i,a}(\{\langle r_i(a, b) \rangle_{b,c}\}_i)/v_{tot} \\ p_b &= \text{Var}_{i,b}(\{\langle r_i(a, b) \rangle_{a,c}\}_i)/v_{tot} \\ p_c &= \text{Var}_{i,c}(\{\langle r_i(a, b) \rangle_{a,b}\}_i)/v_{tot} \\ p_{a+b} &= \text{Var}_{i,a,b}(\{\langle r_i(a, b, c) \rangle_{b,c} - \langle r_i(a, b) \rangle_{b,c} - \langle r_i(a, b) \rangle_{a,c} - \langle r_i(a, b) \rangle_{a,b}\}_i)/v_{tot} \\ p_{b+c} &= \text{Var}_{i,b,c}(\{\langle r_i(a, b, c) \rangle_{b,c} - \langle r_i(a, b) \rangle_{b,c} - \langle r_i(a, b) \rangle_{a,c} - \langle r_i(a, b) \rangle_{a,b}\}_i)/v_{tot} \\ p_{a+c} &= \text{Var}_{i,a,c}(\{\langle r_i(a, b, c) \rangle_{b,c} - \langle r_i(a, b) \rangle_{b,c} - \langle r_i(a, b) \rangle_{a,c} - \langle r_i(a, b) \rangle_{a,b}\}_i)/v_{tot} \\ p_{a+b+c} &= 1 - p_a - p_b - p_c - p_{a+b} - p_{b+c} - p_{a+c} \end{aligned}$$

where  $v_{tot} = \text{Var}_{i,a,b,c}(\{r_i(a, b, c)\}_i)$  is the total variance, “+” sign in the subscript indicates the mixing of several variables.

In **Fig. 3**, we used the network state trajectory after 400 ms (200 ms) of transient period of the perception (production) epoch to do the analysis.

#### S1.4.4 Decoding

We studied two types of nearest-centroid decoders [12]. Given a population state  $\mathbf{f}_0$ , the decoded value  $a_{d,1}$  read-out by Decoder 1 is

$$a_{d,1} = \arg \min_{a \in \mathcal{A}} (\|\mathbf{f}_0 \mathbf{W}^{dec} - \mathbf{f}(a; b_{train}) \mathbf{W}^{dec}\|), \quad (\text{S18})$$

where  $\mathbf{f}(a; b_{train})$  is the population state as a function of variable  $a$  along an iso- $b$  line whose  $b$  value is constantly  $b_{train}$ , and decoding weight  $\mathbf{W}^{dec}$  is the first PC of  $\mathbf{f}(a; b_{train})$ . The decoded value  $a_{d,2}$  read-out by Decoder 2 is

$$a_{d,2} = \arg \min_{a \in \mathcal{A}} (\|\mathbf{f}_0 - \langle \mathbf{f}(a; b_{test}) \rangle_a \mathbf{W}^{dec} - (\mathbf{f}(a; b_{train}) - \langle \mathbf{f}(a; b_{train}) \rangle_a) \mathbf{W}^{dec}\|), \quad (\text{S19})$$

where  $\mathbf{f}(a; b_{test})$  is the iso- $b$  line that  $\mathbf{f}_0$  belongs to, and  $\langle \cdot \rangle_a$  means averaging over  $a$ . From eq.S19, both the mass centers of the two iso- $b$  lines  $\mathbf{f}(a; b_{train})$  and  $\mathbf{f}(a; b_{test})$  are translationally moved to the zero point before  $\mathbf{f}(a; b_{train})$  and  $\mathbf{f}(a; b_{test})$  are projected to the decoding space by  $\mathbf{W}^{dec}$ .

#### S1.4.5 Correlation between decoding error, angle and mixed variance

In **Fig. 4d, f**, we computed the correlation between decoding error (DE), the angle (AG) between the first PCs of the decoded and generalized variables, and the mixed variance (MV) between the decoded and generalized variables. A subtle point here is that AG and MV may also be correlated (see **Fig. 4c, e** for the negative correlation between AG and MV in the production epoch of t-SR), therefore the Pearson’s correlation between DE and AG may be contributed by two pathways: (1) AG influences DE directly; (2) AG influences DE *indirectly* through MV, due to the correlation between AG and MV. Similar situation also exists for the correlation between DE and MV. To investigate the direct correlation and remove the indirect one, we iteratively took the following operation to reduce the correlation between AG and MV: removing a single data point (i.e., the AG and MV of a single training configuration) from the dataset, so that the absolute value of the correlation between AG and MV in the left dataset is minimal. We found that small correlation (with absolute value below 0.05) between AG and MV could usually be obtained after removing 2 or 3 data points from the whole dataset of 30 points (**Figs. S7, S8**). In this way, we got a dataset with small correlation between AG and MV, while at the same time, as large as possible. Pearson’s correlation were then calculated using the left dataset to draw **Figs. 4d, f, S7, S8**.

#### S1.4.6 Firing sequence and network structure

To plot **Fig. 5a, b**, we ordered the peak firing time of strongly active neurons (whose peak firing rates were larger than 2) in the studied epoch, and plotted weight connection as a function of the peak order difference between the post- and pre-synaptic neurons.

To plot **Fig. 5c, d**, we used a more elaborate method to illustrate the network structure underlying t-SR and t-DM. At time  $t_0$  and non-time information  $x_0$  (which may be spatial location or decision choice), we picked a set  $\mathcal{N}(t_0, x_0)$  of strongly active neurons whose firing rates at  $t_0$  and  $x_0$  were larger than a threshold 2 (our result is insensitive to this threshold). We then defined  $T_{peak,i}(t_0, x_0)$  to be the peak time of neuron  $i$  near  $t_0$  at  $x_0$ : if the activity  $f_i(t; x_0)$  of neuron  $i$  decreased

(or increased) with time at time point  $t_0$  and non-time information  $x_0$ , then  $T_{peak,i}(t_0, x_0)$  was the time point of the local maximum of  $f_i(t; x_0)$  before (or after), but most nearest to,  $t_0$ . Iterating over all the possible values of  $x_0$ , we got all the strongly active neurons at time  $t_0$ :  $\mathcal{N}(t_0) = \bigcup_{x_0} \mathcal{N}(t_0, x_0)$ . For neuron  $i$  in  $\mathcal{N}(t_0)$ , we called its preferred non-time information  $x_{prefer}$  to be the value of  $x_0$  that maximized its peak firing rate:  $x_{prefer} = \arg \max_{x_0} f_i(T_{peak,i}(t_0, x_0), x_0)$ . In this way, we classified all the neurons in  $\mathcal{N}(t_0)$  according to their non-time information preference:  $\mathcal{N}(t_0) = \bigcup_{x_0} \mathcal{N}_{prefer}(t_0, x_0)$ , with  $\mathcal{N}_{prefer}(t_0, x_0)$  being the set of neurons that prefer  $x_0$  around time  $t_0$ . We then defined  $T_{peak,i}(t_0, x_{prefer})$  to be the *big peak time* of neuron  $i$  at time  $t_0$ . Given a neuron  $i$  and a set  $\mathcal{N}_{prefer}(t_0, x_0)$  of neurons ( $i$  may or may not belong to  $\mathcal{N}_{prefer}(t_0, x_0)$ ), we ordered their big peak times, and then investigated the recurrent weight from  $i$  to each neuron of  $\mathcal{N}_{prefer}(t_0, x_0)$  (except  $i$  itself if  $i \in \mathcal{N}_{prefer}(t_0, x_0)$ ). In this way, we studied the recurrent weight  $w(o_{post} - o_{pre}, |x_{post} - x_{pre}|)$  as a function of the difference  $o_{post} - o_{pre}$  between the orders of the big peak time of the post- and pre-synaptic neurons and the difference  $|x_{post} - x_{pre}|$  of their preferred non-time information. **Fig. 5c,d** were plotted by averaging  $w(o_{post} - o_{pre}, |x_{post} - x_{pre}|)$  over  $t_0$  and training configurations.

## S2 The relationship between the low dimensionality of the attractor in the delay epoch and the dominance of monotonic neurons

We denote  $\mathcal{M}$  as the manifold of the population states at the end of the delay epoch at different durations  $T$  of the perception epoch (**Fig. 2e**). The first principal component (PC) of  $\mathcal{M}$  explained about 90% of its variance (**Fig. 2g**), and the activities of most neurons changed monotonically with  $T$  in  $\mathcal{M}$  (**Fig. 2j**). To understand the relationship between these two facts, let's consider the extreme case that all neurons are linearly monotonic with  $T$  in  $\mathcal{M}$ , then  $\mathcal{M}$  is a line in the population-state space that can be parameterized as  $[f_1(T), f_2(T), \dots, f_N(T)]^T$ , with  $f_i(T)$  being the activity of the  $i$ th neuron at the end of the delay epoch when the duration of the perception epoch is  $T$ . In this case, PC1 of  $\mathcal{M}$ , which explains 100% of the variance of  $\mathcal{M}$  because  $\mathcal{M}$  is a line, is the following vector with unit length:

$$\pm \frac{1}{\sqrt{\sum_i (f_i(T_{max}) - f_i(T_{min}))^2}} [f_1(T_{max}) - f_1(T_{min}), f_2(T_{max}) - f_2(T_{min}), \dots, f_N(T_{max}) - f_N(T_{min})]^T,$$

where  $T_{min} = 600\text{ms}$  and  $T_{max} = 1200\text{ms}$  are respectively the minimal and maximal values of  $T$  in our simulation, and the  $\pm$  sign indicates that the direction of PC1 is undetermined. If neuron  $i$  monotonically increases (or decreases) with  $T$ , then  $f_i(T_{max}) - f_i(T_{min}) > 0$  (or  $f_i(T_{max}) - f_i(T_{min}) < 0$ ). Apparently, if two neurons  $i$  and  $j$  have the same (or different) monotonicity, then their corresponding elements in PC1 have the same (different) signs. This is indeed what we found in our simulation (**Fig. S2g, h**).

## S3 The geometric meaning of mixed variance

We denote the population state to be  $\mathbf{r} = \{r_1, r_2, \dots, r_N\}$ , where  $r_i$  is the firing rate of the  $i$ th neuron, or in general, the activity projected on the  $i$ th basis vector, say, principal component. Suppose  $\mathbf{r}$  is parameterized by two variables  $a$  and  $b$ , and we subtract the mean value of  $r_i$  so that

$$\mathbb{E}_{a,b}[r_i(a, b)] = 0, \quad (\text{S20})$$

where  $\mathbb{E}_{a,b}[\cdot]$  means the average over  $a$  and  $b$ .

The total variance of  $\mathbf{r}$  is

$$\begin{aligned} v_{tot} &= \text{Var}_{i,a,b}[r_i(a, b)] \\ &= \mathbb{E}_i[\text{Var}_{a,b}[r_i(a, b)]] + \text{Var}_i[\mathbb{E}_{a,b}[r_i(a, b)]] \\ &= \mathbb{E}_i[\text{Var}_{a,b}[r_i(a, b)]], \end{aligned} \quad (\text{S21})$$

where  $\text{Var}_x[\cdot]$  means the variance over variable  $x$ . The first equation is the definition of the total variance, the second equation is from the law of total variance, and the third equation is from eq. S20. Similarly, the variance explained by  $a$  is

$$v_a = \text{Var}_{i,a}[\mathbb{E}_b[r_i(a, b)]] = \mathbb{E}_i[\text{Var}_a[\mathbb{E}_b[r_i(a, b)]]], \quad (\text{S22})$$

and the variance explained by  $b$  is

$$v_b = \text{Var}_{i,b}[\mathbb{E}_a[r_i(a, b)]] = \mathbb{E}_i[\text{Var}_b[\mathbb{E}_a[r_i(a, b)]]] \quad (\text{S23})$$

Now let's study a sufficient condition so that

$$v_{tot} = v_a + v_b, \quad (\text{S24})$$

which means that the mixed variance

$$v_{mix} = v_{tot} - (v_a + v_b) \quad (\text{S25})$$

is zero.

From eqs. S21-S23, a sufficient condition to fulfill eq. S24 is

$$\text{Var}_{a,b}[r_i(a, b)] = \text{Var}_a[\mathbb{E}_b[r_i(a, b)]] + \text{Var}_b[\mathbb{E}_a[r_i(a, b)]] \quad \text{for every } i. \quad (\text{S26})$$

According to the law of total variance,

$$\text{Var}_{a,b}[r_i(a, b)] = \text{Var}_a[\text{E}_b[r_i(a, b)]] + \text{E}_a[\text{Var}_b[r_i(a, b)]] \quad (\text{S27})$$

Therefore, to realize eq. S26, we can set

$$\text{Var}_b[\text{E}_a[r_i(a, b)]] = \text{E}_a[\text{Var}_b[r_i(a, b)]] \quad \text{for every } i. \quad (\text{S28})$$

in other words

$$\text{E}_b[(\text{E}_a[r_i(a, b)] - \text{E}_{a,b}[r_i(a, b)])^2] = \text{E}_a[\text{E}_b[(r_i(a, b) - \text{E}_b[r_i(a, b)])^2]] \quad \text{for every } i \quad (\text{S29})$$

Because  $\text{E}_{a,b}[r_i(a, b)] = 0$ , this equation gives

$$\text{E}_b[(\text{E}_a[r_i(a, b)])^2] = \text{E}_a[\text{E}_b[(r_i(a, b) - \text{E}_b[r_i(a, b)])^2]] \quad \text{for every } i \quad (\text{S30})$$

A sufficient condition to fulfill the equation above is

$$r_i(a, b) - \text{E}_b[r_i(a, b)] = f(b) \quad \text{for every } i, \quad (\text{S31})$$

namely the value of  $r_i(a, b) - \text{E}_b[r_i(a, b)]$  does not depend on  $a$ . This sufficient condition can be easily proved by substituting eq. S31 into eq. S30 and using the fact that  $\text{E}_{a,b}[r_i(a, b)] = 0$ . Now let's try to understand the meaning of eq. S31. Consider four pairs of variables  $(a_1, b_1)$ ,  $(a_2, b_1)$ ,  $(a_1, b_2)$  and  $(a_2, b_2)$ , we have

$$r_i(a_1, b_1) - \text{E}_b[r_i(a_1, b)] = f(b_1) = r_i(a_2, b_1) - \text{E}_b[r_i(a_2, b)] \quad \text{for every } i \quad (\text{S32})$$

$$r_i(a_1, b_2) - \text{E}_b[r_i(a_1, b)] = f(b_2) = r_i(a_2, b_2) - \text{E}_b[r_i(a_2, b)] \quad \text{for every } i \quad (\text{S33})$$

By subtracting eq. S32 from eq. S33, we have

$$r_i(a_1, b_1) - r_i(a_1, b_2) = r_i(a_2, b_1) - r_i(a_2, b_2) \quad \text{for every } i. \quad (\text{S34})$$

This means that between the two iso- $b$  lines in which the values of  $b$  are separately fixed at  $b_1$  and  $b_2$ , the vector that connects the two points representing  $a_1$  is equal to the vector that connects the two points representing  $a_2$ . In other words, these two iso- $b$  lines can be related by translational movement. By rewritten eq.S34 as  $r_i(a_1, b_1) - r_i(a_2, b_1) = r_i(a_1, b_2) - r_i(a_2, b_2)$ , we see that different iso- $a$  lines are also related by translational movement.

From the discussion above, translational relation between different iso- $a$  or iso- $b$  lines is a sufficient condition for zero mixed variance. How about the necessity? In other words, if we observe close-to-zero mixed variance in simulation, how will be the geometry of the iso- $a$  and iso- $b$  lines? We checked this point through simulation. In **Fig. S6**, we show the iso-space lines of several simulation examples, in the perception, delay and production epochs of t-SR task. We see that in examples with small mixed variance, the iso-space lines of different spatial information tend to be parallel and of the same length; whereas in examples with large mixed variance, the iso-space lines may be non-parallel or of very different lengths. Additionally, if iso- $a$  or iso- $b$  lines are translationally related, then Decoder 2 (**eq. S19**) will have perfectly zero generalization error. We found that the generalization error of Decoder 2 is strongly positively correlated with mixed variance (**Figs. 4f, S7, S8**). These results imply that at least in the context of our simulation, mixed variance is a good index to quantify the translational relationship between different iso- $a$  or iso- $b$  lines, or in other words, the parallelogram-likeness of iso- $a$  and iso- $b$  grids (**Fig. 3f, upper left**).

The opposite extreme case that  $v_{mix} = v_{tot}$ , which, from eq.S25, means  $v_a = v_b = 0$ . From eqs. S22, S23, this means that

$$\text{Var}_a[\text{E}_b[r_i(a, b)]] = \text{Var}_b[\text{E}_a[r_i(a, b)]] = 0 \quad \text{for every } i.$$

In other words, the mean value of  $r_i(a, b)$  over  $b$  (i.e.,  $\text{E}_b[r_i(a, b)]$ ) does not depend on  $a$ , and the mean value of  $r_i(a, b)$  over  $a$  (i.e.,  $\text{E}_a[r_i(a, b)]$ ) does not depend on  $b$  neither. This implies that different iso- $a$  (and also iso- $b$ ) lines are strongly intertwined with each other, so that they have the same mean state value. A good example of this case is that every point in the 2-dimensional range of variables  $[a_{min}, a_{max}] \otimes [b_{min}, b_{max}]$  (where  $a_{min}$ ,  $a_{max}$ ,  $b_{min}$  and  $b_{max}$  are the minimal and maximal values of  $a$  and  $b$  respectively) is mapped toward a random point in a state space  $[r_{1,min}, r_{1,max}] \otimes [r_{2,min}, r_{2,max}] \otimes \dots \otimes [r_{n,min}, r_{n,max}]$ : in this case, every iso- $a$  or iso- $b$  dot set of states has the mean value located at the center of the state space  $(\frac{r_{1,min}+r_{1,max}}{2}, \frac{r_{2,min}+r_{2,max}}{2}, \dots, \frac{r_{n,min}+r_{n,max}}{2})$ .

## References

- [1] R. Hattori, K. V. Kuchibhotla, R. C. Froemke, and T. Komiyama, "Functions and dysfunctions of neocortical inhibitory neuron subtypes," *Nat. Neurosci.*, vol. 20, pp. 1199–1208, 2017.
- [2] J. Wang, D. Narain, E. A. Hosseini, and M. Jazayeri, "Flexible timing by temporal scaling of cortical responses," *Nat. Neurosci.*, vol. 21, pp. 102–110, 2018.
- [3] A. E. Orhan and W. J. Ma, "A diverse range of factors affect the nature of neural representations underlying short-term memory," *Nat. Neurosci.*, vol. 22, pp. 275–283, 2019.

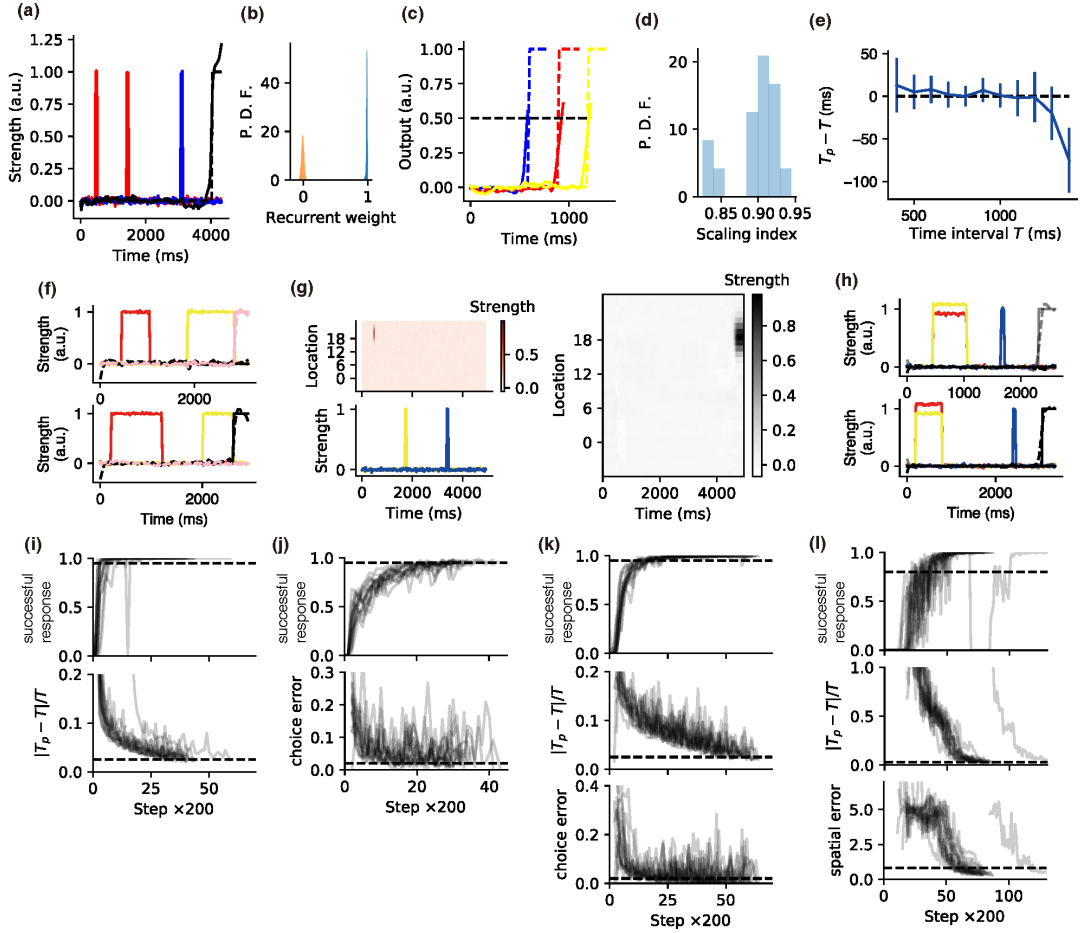


Figure S1: **Performance of the network after training.** (a-e) Interval production (IP) task. (a) An example of the input and output of the network in IP. Red and blue lines: two input channels. Dashed black line: target output. Solid black line: actual output. (b) Probability distribution function (p.d.f) of self-connections (blue) and non-diagonal connections (red) of the recurrent network after training. (c) Three examples of the output in the production epoch of IP, when  $T = 600$  ms (blue), 900 ms (red) and 1200 ms (yellow). Dashed line: target output. Solid line: actual output. The horizontal dashed black line indicates the threshold that the network is regarded to generate a movement in the production epoch when the output rises across this threshold. (d) Distribution of the scaling index of the output across training configurations in the production epoch of IP. (e) The difference between the produced time interval  $T_p$  and the interval  $T$  between the first two pulses in IP as a function of  $T$ . Error bar means standard deviation over 16 training configurations. During training, we set  $T \in [400 \text{ ms}, 1400 \text{ ms}]$ . This panel shows that if after training we set  $T$  to be close to 400 ms,  $T_p$  tends to be larger than  $T$ ; whereas if we set  $T$  to be close to 1400 ms,  $T_p$  tends to be smaller than  $T$ . Therefore, by default, we set  $T \in [600 \text{ ms}, 1200 \text{ ms}]$  for data analysis after training to reduce the bias of  $T_p$ . (f) Two examples of interval discrimination (IC) task. Upper: the case when the duration of the first stimulus is shorter than that of the second stimulus. Lower: the case when the duration of the first stimulus is longer than that of the second stimulus. Red and yellow lines: two input channels. Dashed black and pink lines: two channels of target output. Solid black and pink lines: two channels of actual output. (g) An example of timed spatial reproduction (t-SR) task. Left upper: the pulse with location information from the first input channel. Left lower: the pulses from the second (yellow) and third (blue) input channels. Right: actual output. (h) Two examples of timed decision making (t-DM) task. Upper: when the input from the first channel (red) is weaker than the input from the second channel (yellow), i.e.,  $c < 0$ . Lower: when  $c > 0$ . (i-l) Performance of the network during training. (i) Performance of the network during the training of IP, quantified by the probability to successfully produce time interval (upper) and the relative error of the produced interval (lower). Gray lines indicate individual training configurations. Training stopped as soon as both quantities reach the criterion (horizontal dashed lines). (j) Performance of the network during the training of IC, quantified by the probability to successfully output a choice (upper) and the probability of choice error (lower). (k) Performance of the network during the training of t-SR, quantified by the probability to successfully produce time interval (upper), the relative error of the produced interval (middle) and the spatial error of the output. (l) Performance of the network during the training of t-DM, quantified by the probability to successfully produce time interval (upper), the relative error of the produced interval (middle) and the probability of choice error (lower).

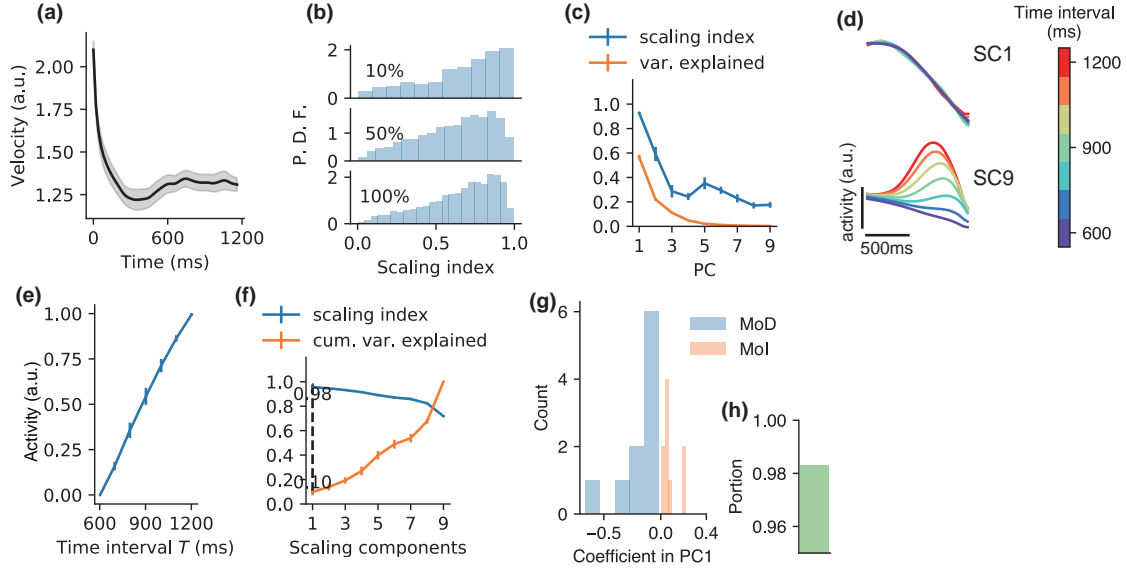


Figure S2: **Interval production task.** (a) Trajectory speed with time in the perception epoch, shaded belt indicating s.e.m. (standard error of mean). (b) Probability distribution function (p.d.f) of scaling indexes of the activities of single neurons in the production epoch, after counting neurons with the top 10% highest activity (upper panel), top 50% (middle panel) and all neurons (lower panel). (c) The scaling index and explained variance of principal components (PC) in the production epoch. (d) We calculated the scaling components in the subspace spanned by the first nine principal components. Shown are the first (upper) and last (lower) scaling component of the production epoch of an example training configuration. Color of lines indicate to-be-produced interval  $T$ . (e) The mean activity of the last scaling component as a function of  $T$ , with the activities when  $T = 600$  ms and  $T = 1200$  ms are respectively normalized to be 0 and 1. (f) Scaling index (blue) and ratio of explained variance (orange) in the subspace spanned by the accumulated scaling components. This panel is in the same style as **Fig. 2n**, except that it analyzes the perception epoch of IP task. (g,h) These two panels explain the relationship between the low dimensionality of manifold  $\mathcal{M}$  at the end of the delay epoch and the dominance of neurons monotonically tuned by  $T$  (Section S2). (g) Histogram of the elements of PC1 of the manifold  $\mathcal{M}$  at the end of the delay epoch at different  $T$ s of an example training configuration. Note that the elements corresponding with monotonically decreasing (MoD) and monotonically increasing (MoI) neurons have different signs. (h) In 16 training configurations, for a given element in PC1 of  $\mathcal{M}$ , it has over 98% probability to have the same sign with most other elements corresponding with neurons of the same type, while have the opposite sign with most other elements corresponding with neurons of the opposite type. In panels **c,e**, error bars indicate s.e.m. over training configurations.

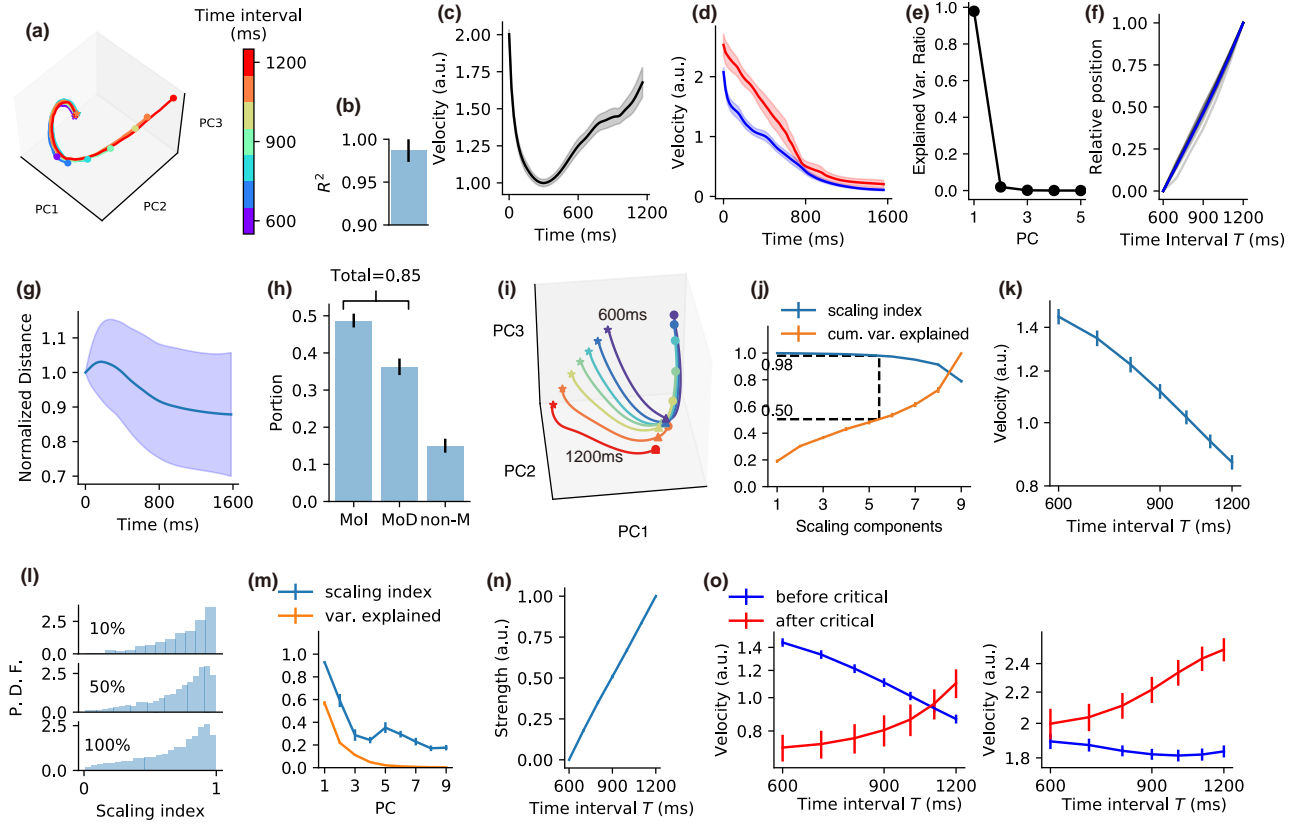


Figure S3: **Interval comparison tasks.** (a-c) Stimulus1 epoch. (a) Population activity in the stimulus1 epoch in the subspace of the first three PCs. Colors indicate the duration  $T$  of the epoch. Stars and circles respectively indicate the starting and ending points of the stimulus1 epoch. (b) Coefficient of determination ( $R^2$ ) that quantifies the overlap of the firing profiles of individual neurons at different  $T$ s, in the same style as **Fig. 2d** in the main text. (c) Trajectory speed as a function of time in the stimulus1 epoch, shaded belt indicating s.e.m. (d-h) Delay epoch. (d) Trajectory speed in the delay epoch when  $T = 600$  ms (blue) and 1200 ms (red), in the same style as **Fig. 2f**. (e) Ratio of explained variance of the first five PCs of manifold  $\mathcal{M}$  at the end of the delay epoch, in the same style as **Fig. 2g**. (f) The position of the state at the end of the delay epoch projected in the first PC of manifold  $\mathcal{M}$  as a function of  $T$ , in the same style as **Fig. 2h**. (g) The distance between two adjacent curves in the delay epoch as a function of time, in the same style as **Fig. 2i**. (h) The portions of monotonically decreasing (MoD), monotonically increasing (MoI), and non-monotonic (non-M) types of neurons at the end of the delay epoch, in the same style as **Fig. 2k**. (i-o) Stimulus2 epoch. (i) Population activity in the stimulus2 epoch in the subspace of the first three PCs. The meanings of color scheme, stars and circles are the same as panel a. Triangles indicate critical points. The duration of stimulus 2 is kept at 1200 ms. (j) Scaling index (blue) and ratio of explained variance (orange) in the subspace spanned by the accumulated scaling components, in the same style as **Fig. 2n**. In this panel and panels k-n, only the trajectories from the beginning of stimulus 2 to the critical points are studied. (k) Trajectory speed in the subspace of the first three scaling components, in the same style as **Fig. 2o**. (l) Probability distribution of the scaling indexes of single neurons, in the same style as **Fig. S2b**. (m) The scaling index and explained variance of principal components, in the same style as **Fig. S2c**. (n) Mean activity of the last scaling component as a function of  $T$ , in the same style as **Fig. S2e**. (o) Left panel: speed of the trajectory before (blue) and after (red) the critical points in the subspace of the first three scaling components (SC). SCs are calculated using the trajectories before the critical points, the red line is plotted by projecting the trajectories after the critical points into the subspace of SCs calculated using those before critical points. Right panel: speed of the trajectory before (blue) and after (red) the critical point in the full population state space.

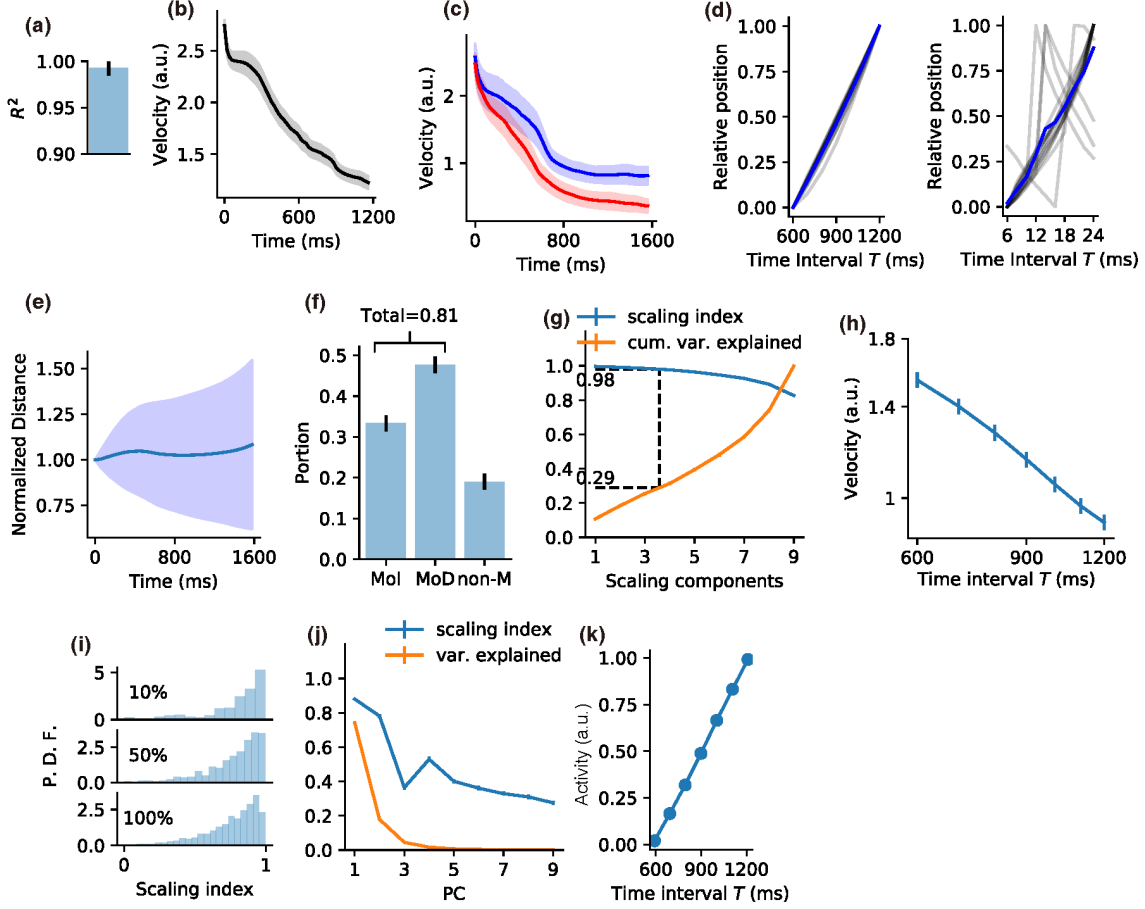


Figure S4: **Timed spatial reproduction task.** (a,b) Perception epoch. (a) Coefficient of determination ( $R^2$ ) that quantifies the overlap of the firing profiles of individual neurons at different  $T$ s in the perception epoch, in the same style as **Fig. 2d**. (b) Trajectory speed as a function of time in the perception epoch, shaded belt indicating s.e.m. (c-f) Delay epoch. (c) Trajectory speed as a function of time in the delay epoch when  $T = 600$  ms (blue) and  $1200$  ms (red), in the same style as **Fig. 2f**. (d) The manifold  $\mathcal{M}$  at the end of the delay epoch are parameterized by both time interval  $T$  between the first two pulses and the spatial location  $x$  of the first pulse. We denote  $\mathcal{M}(T; x_0)$  (or  $\mathcal{M}(x; T_0)$ ) to be the set of dots in  $\mathcal{M}$  at specific location  $x_0$  (or time interval  $T_0$ ). Left panel: the position of the state at the end of the delay epoch projected to the first PC of  $\mathcal{M}(T; x_0)$  as a function of  $T$ , with the position when  $T = 600$  ms (or  $1200$  ms) normalized to be 0 (or 1), in the same style as **Fig. 2h**. Gray curves: results from 16 training configurations, each at a randomly chosen  $x_0$ . Blue curve: mean value averaging over  $x_0$  and training configurations. Right panel: the position of the state in the first PC of  $\mathcal{M}(x; T_0)$ . We see that in most training configurations, the position in  $\mathcal{M}(x; T_0)$  encodes  $x$  continuously and linearly, but big jump happens in some configurations. (e) The distance between two adjacent curves in the delay epoch as a function of time, similar to **Fig. 2i**. (f) The portions of monotonically decreasing (MoD), monotonically increasing (MoI) and non-monotonic (non-M) types of neurons tuned by  $T$  at the end of the delay epoch, in the same style as **Fig. 2k**. (g-k) Production epoch. (g) Scaling index (blue) and ratio of explained variance (orange) in the subspace spanned by the accumulated scaling components in the production epoch, averaging over spatial locations and training configurations, in the same style as **Fig. 2n**. (h) Trajectory speed in the subspace of the first three scaling components in production epoch, in the same style as **Fig. 2o**. (i) Probability distribution of the scaling indexes of single neurons, in the same style as **Fig. S2b**. (j) The scaling index and explained variance of principal components, similar to **Fig. S2c**. (k) Mean activity of the last scaling component, similar to **Fig. S2e**. Error bars representing s.e.m. are much smaller than the plot markers.

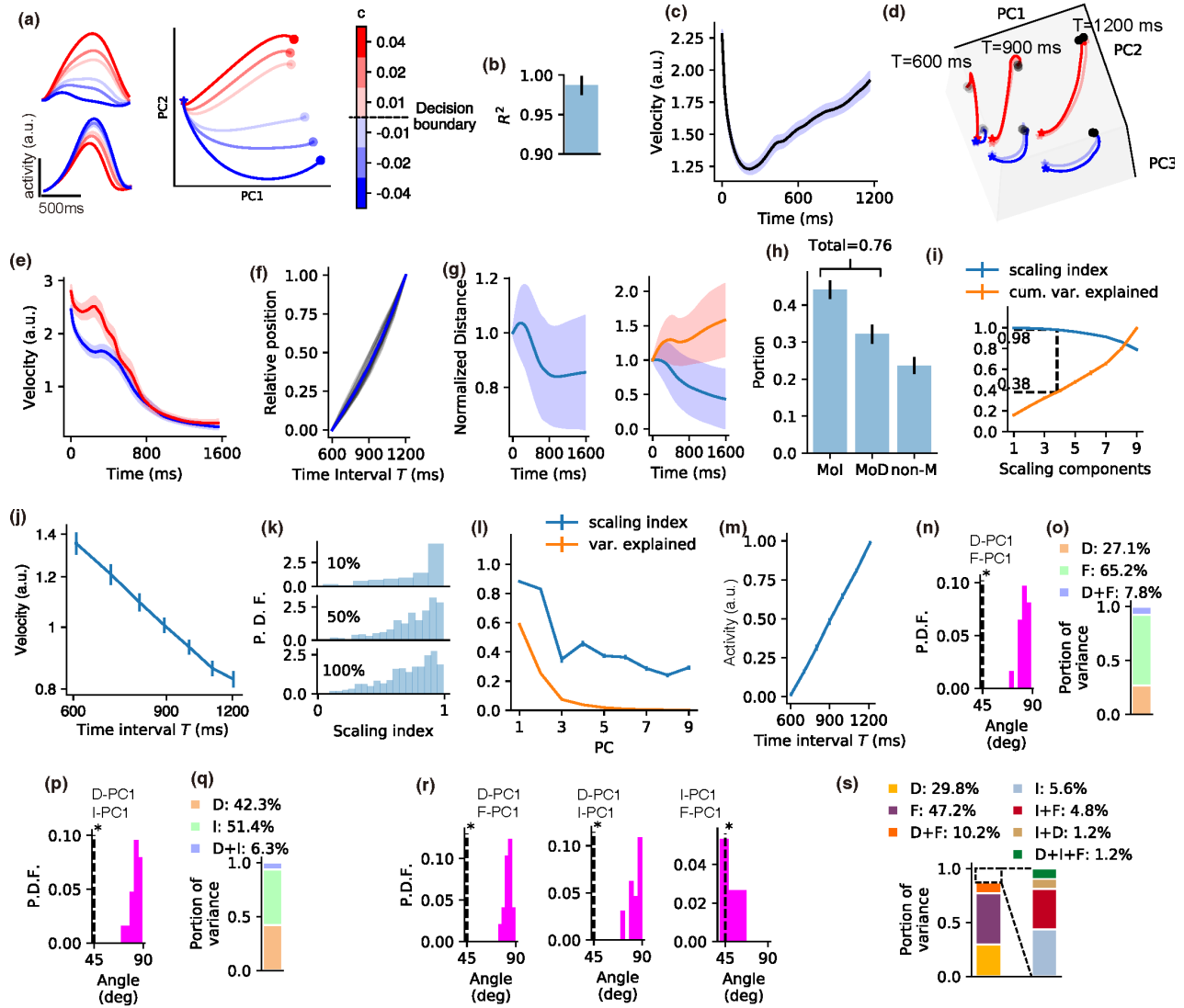


Figure S5: **Timed decision making task.** (a-c) Perception epoch. (a) Left: Firing profiles of two example neurons in the perception epoch. Colors indicate  $c$  value, which is the half difference between the strength of the presented stimuli. Right: Trajectories in the subspace of the first two PCs. Stars and circles respectively indicate the starting and ending points of the perception epoch. (b) Coefficient of determination ( $R^2$ ) that quantifies the overlap of the firing profiles of individual neurons at different  $T$ s in the perception epoch, in the same style as Fig. 2d. (c) Trajectory speed as a function of time in the perception epoch, shaded belt indicating s.e.m. (d-h) Delay epoch. (d) Trajectories in the subspace of the first three PCs. Stars and circles respectively indicate the starting and ending points of the delay epoch. Blackness of circles indicates  $T$  value as annotated. Curve color indicates  $c$  value as indicated in the color map of panel a, only  $c = -0.04, -0.01, 0.01, 0.04$  cases are plotted. (e) Trajectory speed as a function of time in the delay epoch when  $T = 600$  ms (blue) and 1200 ms (red), in the same style as Fig. 2f. (f) The position of the state in the first PC of  $\mathcal{M}(T; d_0)$  as a function of  $T$ , with the position when  $T = 600$  ms (or 1200 ms) normalized to be 0 (or 1), in the same style as Fig. 2h. Here,  $\mathcal{M}(T; d_0)$  represents the set of dots in manifold  $\mathcal{M}$  at the end of the delay epoch at specific decision choice  $d_0$ . (g) The distance between two adjacent curves in the delay epoch as a function of time, in a similar style to Fig. 2i. Left panel: the two adjacent curves have the same  $c$  value, but slightly different  $T$  values. Right panel: the two adjacent curves have the same  $T$  value, but different  $c$  values. In the right panel, blue (orange) curve represents the case when their  $c$  values have the same (different) sign, so that they have the same (different) decision choice. We see that two trajectories representing the same (different) choice tend to get close to (far away from) each other, consistent with the scenario in panel d. (h) The portions of monotonically decreasing (MoD), monotonically increasing (MoI) and non-monotonic (non-M) types of neurons tuned by  $T$  at the end of the delay epoch, in the same style as Fig. 2k. (i-m) Production epoch. (i) Scaling index (blue) and ratio of explained variance (orange) in the subspace spanned by the accumulated scaling components, averaging over  $c$  values and training configurations, in the same style as Fig. 2n. (j) Trajectory speed in the subspace of the first three scaling components, in the same style as Fig. 2o. (k) Probability distribution of the scaling indexes of single neurons, in the same style as Fig. S2b. (l) The scaling index and explained variance of principal components, in the same style as Fig. S2c. (m) Mean activity of the last scaling component, in the same style as Fig. S2e. (n-s) The angle between first parameter-marginalized principal components and mixed variances in the perception (panels n,o), delay (panels p,q) and production epochs (panels r,s). These panels are in the same style as Fig. 3d, e, g-j, except that the non-spatial information is decision choice.

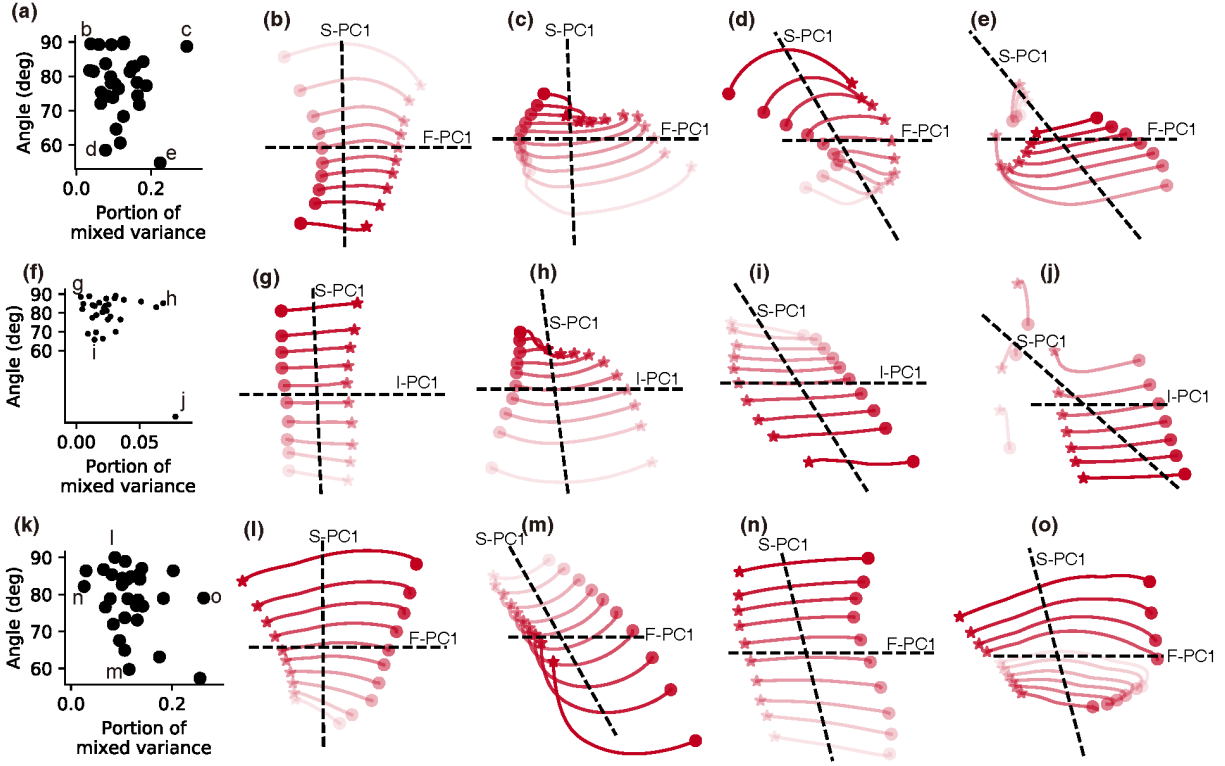


Figure S6: **Examples that illustrate the geometry of the coding combination of temporal and spatial information in t-SR.** (a-e) Perception epoch. (a) Each dot represents the angle between F-PC1 and S-PC1 as well as their mixed variances in the perception epoch (after 400 ms of transient period) of t-SR in a training configuration. (b-e) Iso-space lines in the subspace spanned by F-PC1 and S-PC1, in the training configurations indicated in panel a. Stars indicate the points after 400 ms of transient period from the beginning of the perception epoch, and circles indicate the ending points of the perception epoch. Redness from light to strong indicates the spatial locations  $x = 0, 2, 4, \dots, 18$ . (f-j) The same as panels a-e, except for showing the iso-space lines in the manifold  $\mathcal{M}$  at the end of the delay epoch, in the subspace spanned by the first time-interval PC (I-PC1) and S-PC1. Stars and circles indicate  $T = 600$  ms and 1200 ms cases respectively. (k-o) The same as panels a-e, except that the iso-space lines in the production epoch are shown. Stars indicate the points after 200 ms of transient period from the beginning of the production epoch, and circles indicate the ending points of the production epoch.

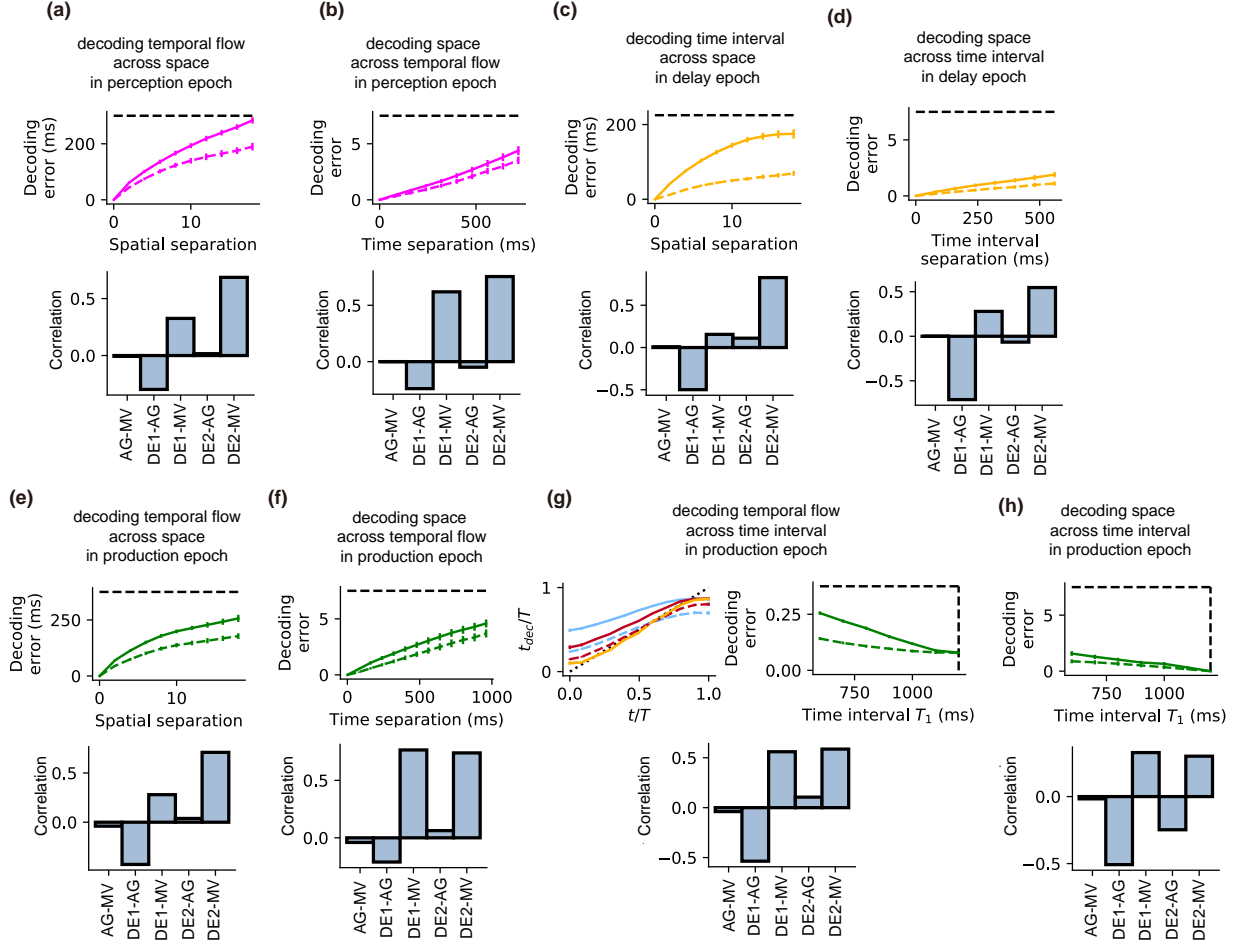


Figure S7: **Decoding generalizability in t-SR.** (a-b) Perception epoch. (a) Upper: decoding error as a function of  $|x_{train} - x_{test}|$ , after Decoder 1 (solid line) or Decoder 2 (dashed line) is trained to read the time elapsed from the beginning of the perception epoch (i.e., temporal flow) using the state trajectory at spatial location  $x_{train}$ , and then tested at spatial location  $x_{test}$ , in the same style as **Fig. 4g**. Horizontal dashed line indicates chance level, supposing the decoder works by random guess. Lower: The correlations between the angle (AG) between the first temporal-flow PC and the first spatial PC, the mixed variance (MV) between temporal flow and spatial information, the error of Decoder 1 (DE1) and the error of Decoder 2 (DE2), in the same style as **Fig. 4d, f**. Note that the correlation between AG and MV is approximately zero, see **Section S1.4.5** for this point. (b) Upper: Decoding error as a function of  $|t_{train} - t_{test}|$ , after Decoder 1 (solid line) or Decoder 2 (dashed line) is trained to read the spatial location at time  $t_{train}$  after the beginning of the perception epoch, and then tested at time  $t_{test}$ . Lower: Correlations between AG, MV, DE1 and DE2. (c-d) Delay epoch. (c) Similar to panel a, except for decoding time interval across spatial information using the state in manifold  $\mathcal{M}$  at the end of the delay epoch. (d) Decoding spatial information across time interval using the states in manifold  $\mathcal{M}$  at the end of the delay epoch. (e-h) Production epoch. (e) Decoding temporal flow across spatial information in the production epoch. The decoder was trained using  $\mathbf{r}(t; x_{train}, T_0)$  and tested using  $\mathbf{r}(t; x_{test}, T_0)$ , where  $\mathbf{r}(t; x_0, T_0)$  represents the population activity as a function of  $t$  at specific spatial information  $x_0$  and time interval  $T_0$ .  $T_0 = 1200$  ms in this panel and panels f. (f) Decoding space across temporal flow in the production epoch. The decoder was trained using  $\mathbf{r}(x; t_{train}, T_0)$  and tested using  $\mathbf{r}(x; t_{test}, T_0)$ , where  $\mathbf{r}(x; t_0, T_0)$  represents the population activity as a function of spatial information  $x$  at specific time point  $t_0$  and time interval  $T_0$ . (g) Decoding temporal flow across time interval in the production epoch. The decoder was trained using  $\mathbf{r}(t; T_{train}, x_0)$  and tested using  $\mathbf{r}(t; T_{test}, x_0)$ . The results are averaged over  $x_0 \in [0, 20]$ . Upper left: The decoded value  $t_{dec}$  as a function of the time  $t$  elapsed from the beginning of the production epoch, after Decoder 1 (solid line) or Decoder 2 (dashed line) was trained to read  $t$  at  $T = 1200$  ms, and then tested at  $T = 600$  ms (blue), 900 ms (red) and 1200ms (yellow). The dashed line indicates perfect temporal scaling. Upper right: Decoding error as a function of  $T$ , after a decoder is trained to read scaled temporal flow  $t/T$  at  $T = 1200$  ms (indicated by the vertical dashed line), and then tested at  $T = T_1$ . Lower: correlations. (h) Decoding space across time interval in the production epoch. The decoder was trained using  $\langle \mathbf{r}(x; T_{train}, t_0) \rangle_{t_0}$  and tested using  $\langle \mathbf{r}(x; T_{test}, t_0) \rangle_{t_0}$ , where  $\langle \cdot \rangle_{t_0}$  means averaging over temporal flow  $t_0$ .

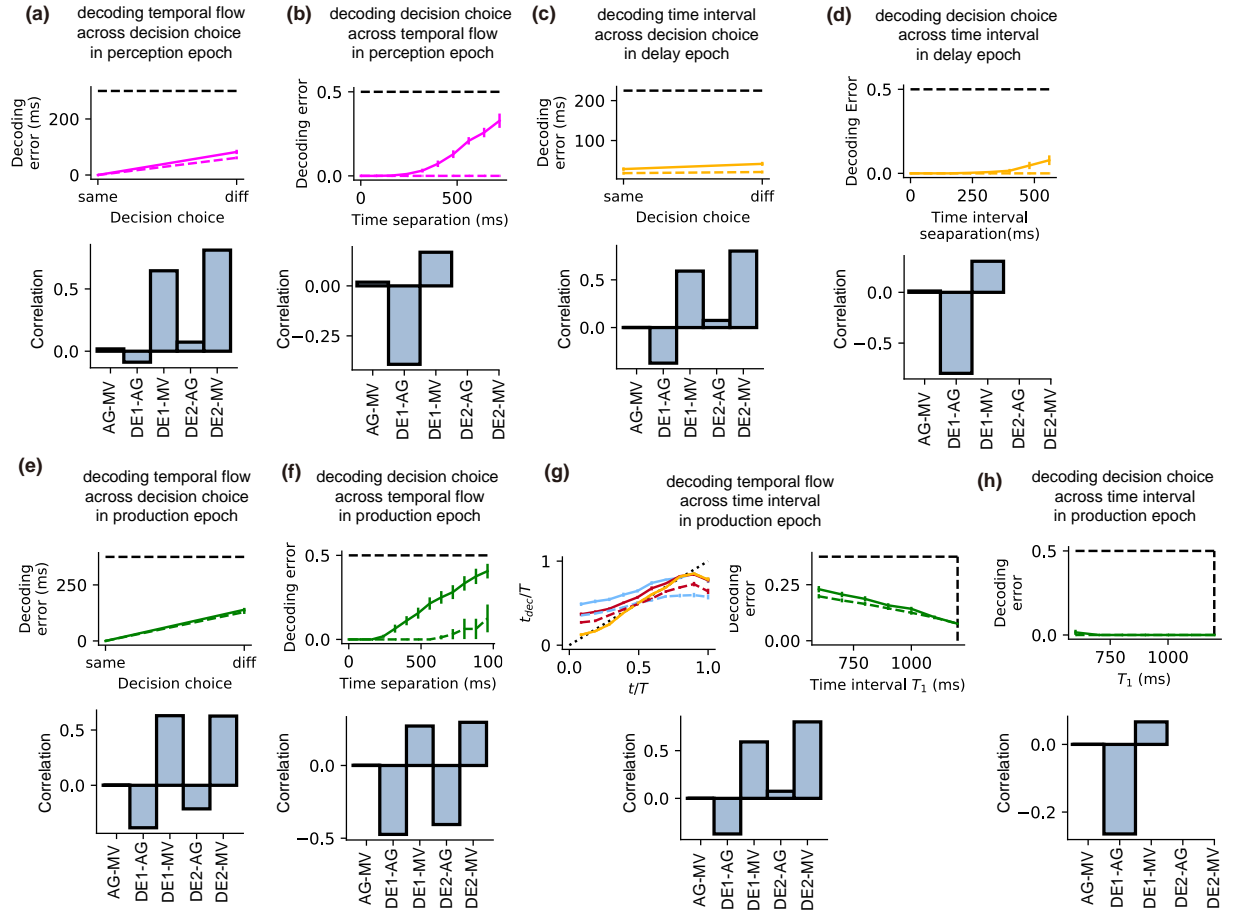


Figure S8: **Decoding generalizability in t-DM.** All panels are in the same style as **Fig. S7**, except that the non-temporal information in t-DM is the decision choice. Note that in some panels (lower panels of **b**, **d**, **h**), the correlation between DE2 and AG as well as the correlation between DE2 and MV are absent. The reason is that in these cases, the decoding error is perfectly zero in all training configurations, so the correlation is undefined.

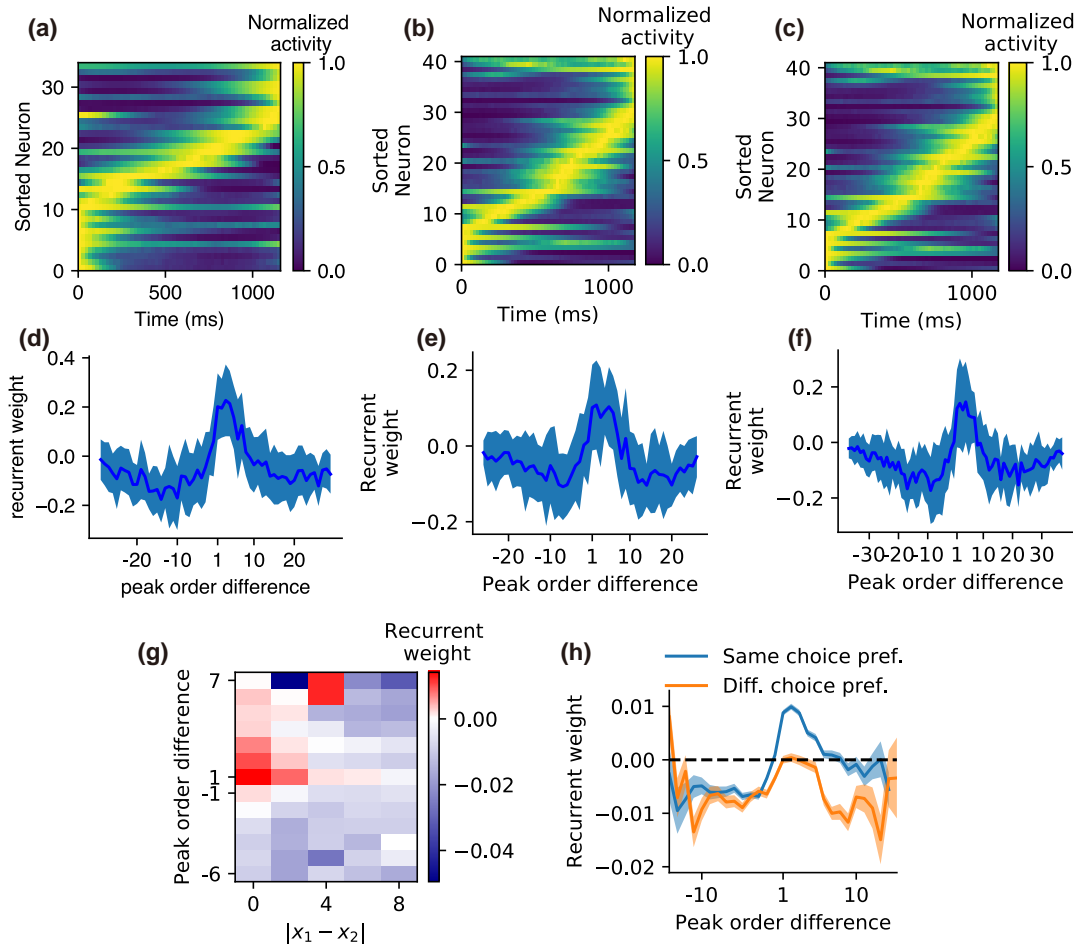


Figure S9: **Sequential activity and network structure.** (a) The neuronal activity (with maximum normalized to 1) in the production epoch of IP task in an example training configuration, sorted according to peak time. (b, c) The same as panel a, but for the stimulus1 (panel b) or stimulus2 (panel c) epoch of IC. (d) Mean (solid line) and s.d. (shaded belt) of the recurrent weights as a function of the peak order difference between post- and pre-synaptic neurons in the production epoch of IP. (e, f) The same as panel d, but for the stimulus1 (panel e) or stimulus2 (panel f) epoch of IC. (g) Recurrent weight as a function of the difference  $|x_1 - x_2|$  between the preferred spatial locations of post- and pre-synaptic neurons and their peak order difference in the production epoch of t-SR. (h) Recurrent weight as a function of peak order difference in the sequence of neurons with the same (blue) or different (orange) preferred decision choices in the production epoch of t-DM. Shaded belt indicates s.e.m.

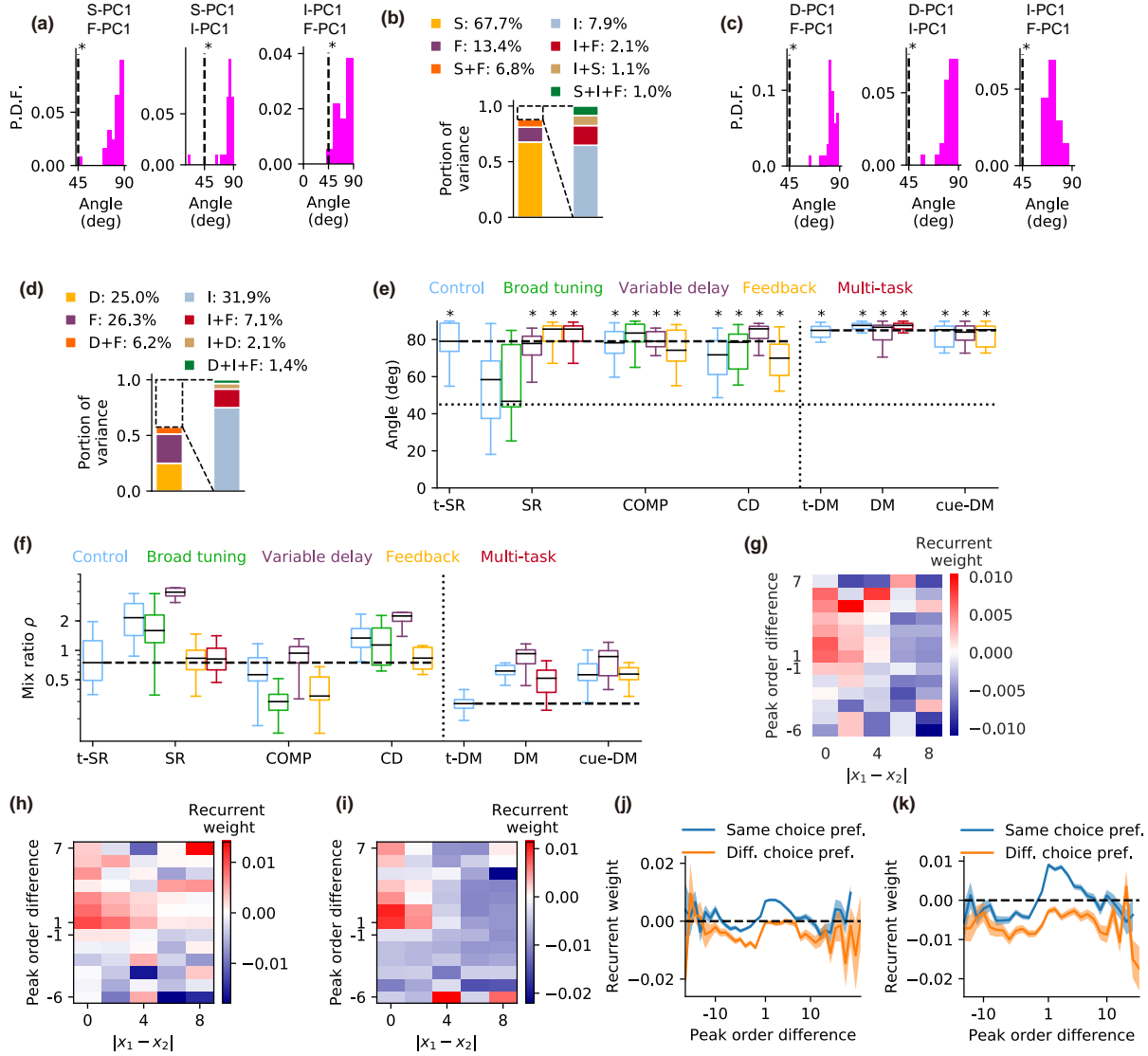


Figure S10: **Coding geometry and network structure in the absence of timing task requirement.** (a,b) The angle and mixed variance between the subspaces coding temporal flow (F), time interval (I) and spatial information (S) in the delay epoch of t-SR, in the same style as **Fig. 3i, j**. (c,d) Similar to panel a,b, except for the delay epoch of t-DM, where the non-temporal information is decision choice (D). (e) The angle between the first temporal-flow PC and the first spatial (in t-SR, SR, COMP and CD) or decision-choice (in t-DM, DM and cue-DM) PC. Whisker plots: center line, median; box, 25th to 75th percentiles; whiskers,  $\pm 1.5 \times$  the interquartile range. In t-SR and t-DM, the perception epoch is studied; in SR, COMP and CD, the delay epoch is studied; in DM and cue-DM, the stimulus-presentation epoch is studied. Asterisk indicates significant ( $p < 0.05$ ) larger than  $45^\circ$  (t test). The horizontal dotted line indicates  $45^\circ$ , the vertical dotted line separates the spatial task group (t-SR, SR, COMP and CD) from the decision-making task group (t-DM, DM and cue-DM). The two horizontal dashed line indicate the median values of t-SR and t-DM (which respectively are the only timing task in each group) separately. (f) Mixed ratio  $\rho$  in several tasks, where  $\rho = v_{\min} / \min(v_{\text{time}}, v_{\text{non-time}})$ , where  $v_{\min}$  is the mixed variance,  $v_{\text{time}}$  and  $v_{\text{non-time}}$  are the variance explained by temporal and non-temporal information separately. (g) Recurrent weight as a function of the difference  $|x_1 - x_2|$  between the preferred spatial locations of post- and pre-synaptic neurons and their peak order difference in the delay epoch of SR. (h) The same as panel g, except for COMP. (i) The same as panel g, except for CD. (j) Recurrent weight as a function of peak order difference in the sequence of neurons with the same (blue) or different (orange) preferred decision choices during the presentation of the stimuli in cue-DM. Shaded belt indicates s.e.m. (k) The same as panel j, except for DM.

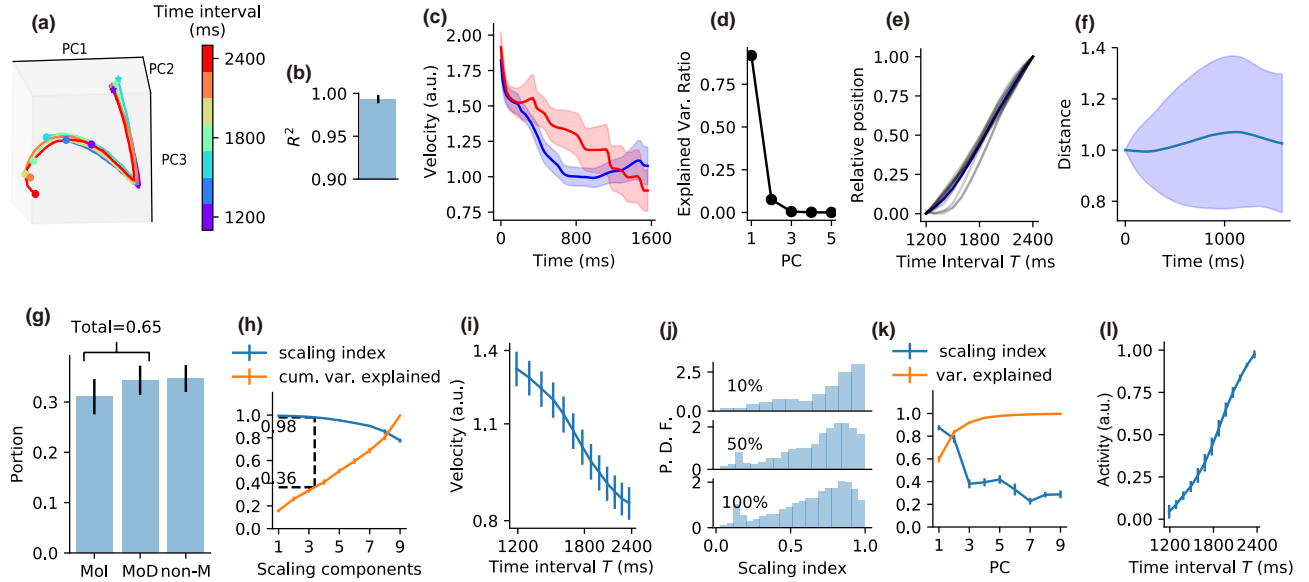


Figure S11: **Dynamics of the network when trained to produce long time intervals.** (a-b) Perception epoch. (a) Population activity in the perception epoch in the subspace of the first three PCs. Colors indicate the time interval  $T$ . Stars and circles respectively indicate the starting and ending points of the perception epoch. (b) Coefficient of determination ( $R^2$ ) that quantifies the overlap of the firing profiles of individual neurons at different  $T$ s in the perception epoch, in the same style as **Fig. 2d**. (c-g) Delay epoch (c) Trajectory speed in the delay epoch when  $T = 1200$  ms (blue) and 2400 ms (red), in the same style as **Fig. 2f**. (d) Ratio of explained variance of the first five PCs of manifold  $\mathcal{M}$  at the end of the delay epoch, in the same style as **Fig. 2g**. (e) The position of the state at the end of the delay epoch projected in the first PC of manifold  $\mathcal{M}$  as a function of  $T$ , in the same style as **Fig. 2h**. (f) The distance between two adjacent curves in the delay epoch as a function of time, in the same style as **Fig. 2i**. (g) The portions of monotonically decreasing (MoD), monotonically increasing (MoI) and non-monotonic (non-M) types of neurons tuned by  $T$  at the end of the delay epoch, in the same style as **Fig. 2k**. (h-l) Production epoch. (h) Scaling index (blue) and ratio of explained variance (orange) in the subspace spanned by the accumulated scaling components, in the same style as **Fig. 2n**. (i) Trajectory speed in the subspace of the first three scaling components, in the same style as **Fig. 2o**. (j) Probability distribution of the scaling indexes of single neurons, in the same style as **Fig. S2b**. (k) The scaling index and explained variance of principal components, in the same style as **Fig. S2c**. (l) Mean activity of the last scaling component as a function of  $T$ , in the same style as **Fig. S2e**.

- [4] G. R. Yang, M. R. Joglekar, H. F. Song, W. T. Newsome, and X.-J. Wang, “Task representations in neural networks trained to perform many cognitive tasks,” *Nat. Neurosci.*, vol. 22, pp. 297–306, 2019.
- [5] Q. V. Le, N. Jaitly, and G. E. Hinton, “A simple way to initialize recurrent networks of rectified linear units,” *arXiv* <https://arxiv.org/abs/1504.00941>, 2015.
- [6] A. Goel and D. V. Buonomano, “Temporal interval learning in cortical cultures is encoded in intrinsic network dynamics,” *Neuron*, vol. 91, pp. 1–8, 2016.
- [7] C. J. MacDonald, K. Q. Lepage, U. T. Eden, and H. Eichenbaum, “Hippocampal ‘time cells’ bridge the gap in memory for discontinuous events,” *Neuron*, vol. 71, pp. 737–749, 2011.
- [8] R. H. R. Hahnloser, A. A. Kozhevnikov, and M. S. Fee, “An ultra-sparse code underlies the generation of neural sequence in a songbird,” *Nature*, vol. 419, pp. 65–70, 2002.
- [9] E. Pastalkova, V. Itskov, A. Amarasingham, and G. Buzsáki, “Internally generated cell assembly sequences in the rat hippocampus,” *Science*, vol. 321, pp. 1322–1327, 2008.
- [10] C. D. Harvey, P. Coen, and D. W. Tank, “Choice-specific sequences in parietal cortex during a virtual-navigation decision task,” *Nature*, vol. 484, pp. 62–68, 2012.
- [11] D. Kobak, W. Brendel, C. Constantinidis, C. E. Feierstein, A. Kepecs, Z. F. Mainen, X.-L. Qi, R. Romo, N. Uchida, and C. K. Machens, “Demixed principal component analysis of neural population data,” *eLife*, vol. 5, p. e10989, 2016.
- [12] J. D. Murray, A. Bernacchia, N. A. Roy, C. Constantinidis, R. Romo, and X.-J. Wang, “Stable population coding for working memory coexists with heterogeneous neural dynamics in prefrontal cortex,” *Proc. Natl. Acad. Sci. USA*, vol. 114, pp. 394–399, 2017.